USGS
science for a changing world

Comparison of Phase Velocities from Array Measurements of Rayleigh Waves Associated with Microtremor and Results Calculated from Borehole Shear-Wave Velocity Profiles

By Hsi-Ping Liu[1], David M. Boore[1], William B. Joyner[1], David H. Oppenheimer[1], Richard E. Warrick[1], Wenbo Zhang[2], John C. Hamilton[1], *and* Leo T. Brown[3]

[1] U.S. Geological Survey, 345 Middlefield Road, Menlo Park, California 94025
[2] Present address: Beijing Strong-Motion Observation Center, Institute of Engineering Mechanics, China Seismological Bureau, Beijing, 100080, China
[3] Present address: Geovision Geophysical Services, 1785 Pomona Road, Suite B, Corona, California 92880

ABSTRACT

Shear-wave velocities (V_S), which are widely used for earthquake ground-motion site characterization studies, are now largely obtained using borehole methods. Drilling holes, however, is expensive. Surface methods are less expensive for obtaining V_S information, but not many comparisons with direct borehole measurements have been made. Because different assumptions are used in data interpretation of each surface method, and because public safety is involved in site characterization for engineering structures, it is important to validate the surface methods by additional comparisons with borehole measurements. We compare results obtained from a particular surface method (array measurement of surface waves associated with microtremor) with results obtained from borehole methods. Using a ten-element nested-triangular array of 100-m aperture, we measured surface-wave phase velocities at two California sites, Garner Valley near Hemet and Hollister Municipal Airport. The Garner Valley site is located at an ancient lake bed where water-saturated sediment overlies decomposed granite on top of granite bedrock. Our array was deployed at a location where seismic velocities had been determined to a depth of 500 m by borehole methods. At Hollister, where the near-surface sediment consists of clay, sand, and gravel, we determined phase velocities using an array located close to a 60-m deep borehole where downhole velocity logs already exist. Because we want to assess the measurements uncomplicated by uncertainties introduced by the inversion process, we compare our phase-velocity results with the borehole V_S depth profile by calculating fundamental-mode Rayleigh-wave phase velocities from an earth model constructed from the borehole data. For wavelengths <~2 times of the array aperture at Garner Valley, phase-velocity results from array measurements agree with the calculated Rayleigh-wave velocities to better than 11%. Measurement errors become larger for wavelengths >2 times of the array aperture. At Hollister, the measured phase velocity at 3.9 Hz (near the upper edge of the microtremor frequency band) is within 20% of the calculated Rayleigh-wave velocity. Because shear-wave velocity is the predominant factor controlling Rayleigh-wave phase velocities, these comparisons suggest that this non-intrusive method can provide V_S information adequate for ground motion estimation provided two conditions are met. These conditions are: (1) the site velocity structure can be approximated by a horizontally-layered structure at least on the size of the seismic array, and (2) when the surface wavelength is <~2 times of the array aperture.

INTRODUCTION

Shear-wave velocity information in soil and rock are widely used in earthquake engineering (*e.g.*, Kramer, 1996). For example, Boore *et al.* (1997) predicted empirical strong ground motion using V_S data. Site coefficients for building codes (NEHRP 1997; ICBO 1997) require such information. Stokoe and Nazarian (1985) characterized liquefaction potential and Charlie *et al.* (1985) embankment stability using V_S. Graves *et al.* (1985) used V_S data as input for numerical simulation of basin response.

V_S data are now largely obtained using borehole methods. However, the drilling and cuttings disposal costs for these methods are high. Compared to direct borehole methods, non-intrusive surface methods for obtaining V_S information cost much less. Such surface methods include refraction and inversion of Rayleigh-wave phase velocities using controlled sources [*e.g.*, the Spectral-Analysis-of-Surface-Waves (SASW) method, Stokoe *et al.*, 1994], explosions (*e.g.*, Malagnini *et al.*, 1997), or microtremor (*e.g.*, Horike, 1985; Milana *et al.*, 1996; Kawase *et al.*, 1998). Because different assumptions are used in data interpretation of each surface method, and each method has its own limitations, it is important to validate the surface methods by additional comparisons with borehole measurements. More comparisons are also required from a practical point of view because public safety is involved in site characterization for engineering structures.

There have been a few comparisons of the SASW method with borehole measurements (Stokoe and Nazarian, 1985; Brown, 1998; Brown *et al.*, 2000). The purpose of this paper is to compare velocity results obtained from another surface method, array measurements of surface waves associated with microtremor, with those obtained from borehole methods. Because we want to assess the measurements uncomplicated by uncertainties introduced by the inversion process, we have chosen to use phase velocities as the basis for comparison rather than the shear-wave velocities obtained by inverting the phase velocities. A complete assessment of shear-wave velocities obtained from surface-wave methods would, of course, require consideration of the uncertainties introduced by inversion.

We have conducted array measurements at two California sites where borehole velocity data already exist. The two sites are located at Garner Valley near Hemet (where borehole velocities have been determined to a depth of 500 m) and at Hollister Municipal Airport (where borehole velocities have been determined to a depth of 60 m). We analyzed our data using both the frequency-wavenumber power-spectrum method and the high-resolution frequency-wavenumber method. We first describe the experiments and results for the two sites. We then show results of numerical simulation using synthetic ground noise. Details of field experiments and data analysis are given.

GARNER VALLEY

Site and Array Location

Figure 1 shows the location of the 100-m aperture array. The site is located on an ancient lake bed where water-saturated sediment (20-m thick) overlies decomposed granite (67-m thick) on top of the granite bedrock (Steidl *et al.*, 1996). Seismic velocities at the site have been measured using borehole suspension loggers to 500-m depth. In addition, interval velocities have been determined from earthquake arrival times at a 6-level three-component borehole accelerometer array; the deepest accelerometer is located at a depth of 220 m and the surface projection of the 6-level vertical array is covered by our array. We have adopted for the site the V_S model and geologic log of Steidl (Figure

2) who has access to the borehole logs and the earthquake data (Jamison H. Steidl, University of California at Santa Barbara, 1997, written communication).

The sources of microtremor are presumably traffic on local highways and in the local campgrounds. However, whenever a car came within sight on Highway 74 (Pines to Palms Highway in Figure 1), ground motions produced by that car could not be used for array measurements. The reason is that, in less than 40.96 seconds (the record length used in the data analysis), that car would be so close to our array that its vibrations would saturate all microtremor recordings.

Experimental Arrangement

The array consists of ten Mark Products[¶] Model L-4C 1 Hz vertical-component geophones, calibrated using a release test (*e.g.*, Asten, 1977) and a phase-ellipse test (*e.g.*, Liu and Peselnick, 1986), and adjusted to 0.7 of critical damping by shunt resistors.

Prior to field experiments, we estimated the error in phase-velocity measurement due to differences in geophone phase characteristics by the following procedure. Geophones were compared in pairs by placing two geophones side-by-side on the floor of our basement laboratory. We recorded ground noise for 60 seconds and then computed the Fourier phase spectrum of the records. At frequency f a phase difference, $(\Delta\phi)_{ij}$, between the phase spectrum of geophone i and of geophone j is equivalent to a time error in velocity measurement of $(\Delta t)_{ij} = (\Delta\phi)_{ij}/(2\pi f)$. For two geophones separated by distance l_{ij} in an array experiment, the fractional error in phase velocity measurement for waves propagating in the direction defined by these two geophones is $(\Delta c)_{ij}/c = -(\Delta t)_{ij}/t = -c(\Delta\phi)_{ij}/(2\pi l_{ij}f)$. From our laboratory test, $|(\Delta\phi_{ij})| = 4.2\times10^{-2}$ radians at 1 Hz. The corresponding error in phase-velocity measurement using a pair of geophones over a distance of 100 m is $\Delta c/c = 0.09$, assuming $c \cong 1.3$ km/s at 1 Hz. Because in general c decreases with increasing f, this fractional error decreases at higher frequencies. We analyze our field data only for frequencies ≥ 1 Hz. When ten geophones are placed in an array, it is difficult to evaluate exactly the fractional error for the entire array for the following two reasons. (1) The effective separation between two geophones depends on the back azimuth of a plane wave and there are multi-azimuth surface waves associated with ground noise. (2) Each pair of geophones contributes differently to the determination of phase velocity by an array.

In the field, we laid out the geophones in a nested-triangular configuration using a Theomat Wild T2002 electronic total station to control sensor location. Position error, introduced when geophones were emplaced in soil, is ±2 cm. The nested-triangular configuration, shown in Figure 1, is representative of all our arrays.

[¶] Use of commercial product name does not imply endorsement by the U.S. Geological Survey

Each geophone, embedded in the surface soils, was hard-wired to one of two USGS General Earthquake Observation System (GEOS) digital recorders (Borcherdt *et al.*, 1985), with five geophones connected to one recorder. Sampling rate was set at 200 samples/s and the low-pass filter cutoff frequency at 33 Hz. Timing of the two recorders, controlled by an external clock, was synchronized to better than 0.1 ms.

Microtremor Measurements

Measurements were made on June 24, 1997 between 3:47 p.m. and 7:53 p.m. local time (97:175:22:47 to 97:176:02:53 UTC). The time period was chosen based on a previous site-monitoring experiment which determined that microtremor from car traffic decreased by an order of magnitude after 10 p.m. local time. The microtremor were then dominated by a higher-frequency noise, presumably due to a local electric generator. Had we conducted the experiment after 10 p.m., we would have lost most of the traffic-generated microtremor. Amplifier gain for the geophones was set at 78 dB.

Data

Thirty-one separate time segments of ~60-seconds duration were recorded. Figure 3*a* shows microtremor recorded by the Garner-Valley array at 4:22 p.m. on June 24, 1997; these microtremor records are very similar to each other. In contrast, the microtremor shown in Figure 3*b*, recorded at 6:17 p.m. on the same day, are less similar to each other.

Data Analysis

We assume that the microtremor wavefield consists of surface waves propagating on the surface of a laterally homogeneous plane-layered earth.

Array analysis of seismic data are discussed in, *e.g.*, Capon *et al.* (1967), Lacoss *et al.* (1969), Capon (1969, 1973), and Aki and Richards (1980, p. 619–625). We have analyzed our data from 2.4 to 5.9 Hz using both the frequency-wavenumber power-spectrum or beam-forming (BF) method and the high-resolution-frequency-wavenumber spectrum-analysis (HRFK) method using computer codes similar to those used by Liaw (1977) and Oppenheimer and Iyer (1980). A summary of both methods and their implementation are presented in Appendix A.

Results

Fourier Spectra. Figures 4*a* and 4*b* show the Fourier spectra of the microtremor shown in Figures 3*a* and 3*b*, respectively. These spectra have significant amplitudes from ~5 Hz to beyond 10 Hz. Reflecting the microtremor records of Figure 3, the spectra in Figure 4*a* are quite similar to each other, whereas in contrast, those in Figure 4*b* are less similar to each other. There are obvious differences among the velocity spectra shown in Figure 4*b*, *e.g.*, between those of station #3 and station #10. One possible cause for these differences is the incoherent noise generated by wind action on vegetation (Capon, 1973). However,

because the wind was dying down when the data were obtained, it is more likely that these differences are caused by interference from multi-azimuth surface waves generated by more distant cars. For illustration, consider two surface sine waves of the same frequency and amplitude but travelling in opposite directions. The resulting standing waves have zero amplitude at the nodal lines but maximum amplitude at the anti-nodal lines. The spectra at nodal lines and at anti-nodal lines are very different. Multi-azimuth surface waves decrease coherence, produce differences in spectra among the array records, and cause error in phase velocity measurements. Phase-velocity results determined from multi-azimuth synthetic ground noise are shown in Appendix B.

Power-Spectrum Contours. Figure 5a shows $\left|\tilde{P}(s_x,s_y,\omega)\right|$ at 4.6 Hz from the microtremor records shown in Figure 3a, where $\tilde{P}(s_x,s_y,\omega)$ is the power output of the HRFK filter as a function of wave-slowness components s_x and s_y for a specific angular frequency ω. Two contour peaks are resolved with the highest peak at a slowness of $s = 2.43\,\text{s}\,/\,\text{km}$ and a back azimuth of $\psi = 291.5\,^{\circ}$. In contrast, the plot for $\left|\tilde{P}(s_x,s_y,\omega)\right|$ at the same frequency for the microtremor records of Figure 3b, shown in Figure 5b, displays five resolved peaks (the highest peak is at a slowness of $s = 2.55\,\text{s}\,/\,\text{km}$ and a back azimuth of $\psi = 119.1\,^{\circ}$). These power-spectrum contours substantiate our interpretation that the lack of similarity among the spectra in Figure 4b as compared to those in Figure 4a is caused by multi-azimuth surface waves.

Figure 6a shows $\left|\hat{P}(s_x,s_y,\omega)\right|$ at 4.6 Hz for beams formed from the records in Figure 3a. Its peak occurs at a slowness of $s = 2.29\,\text{s}\,/\,\text{km}$ and a back azimuth of $\psi = 310.9\,^{\circ}$. In contrast to contours with two resolved peaks by the HRFK method (Figure 5a), the contours by the BF method in Figure 6a has one broad peak.

Figure 6b shows the contour plot calculated from synthetic microtremor records simulating a plane wave of $s = 2.29\,\text{s}\,/\,\text{km}$ and $\psi = 310.9\,^{\circ}$. As demonstrated in APPENDIX B, all plane waves traveling with the same slowness vector $(s_x^{(1)}, s_y^{(1)})$ have the same $\hat{P}(s_x,s_y,\omega)$, proportional to a displaced array weight function, $W(s_x^{(1)}, s_y^{(1)}, \omega)$, regardless of the time variation of the plane waves. It is apparent that the contour pattern in Figure 6a is different from that of a single plane wave as shown in Figure 6b. One possible explanation is that the contours in Figure 6a represent the superposition of several displaced array functions.

Phase Velocity and Back-Azimuth Results from Field Measurements; Comparison of Velocity Results with Calculated Rayleigh-Wave Velocities Based on Earth Models Constructed from Borehole Logs and Earthquake Data. For each contour plot derived from microtremor records of 40.96-s duration from 10 geophones, we determine the phase-velocity (inverse of slowness) and back-azimuth given by the highest contour peak. Phase velocities from 2.4 to 5.9 Hz from 31 measurements by the HRFK method are

5

shown in Figure 7a. Light error bar represents ± 1 standard deviation of the phase velocity and heavy error bar represents ± 1 standard error of the mean. The error-bar size increases at low frequencies. Phase velocities determined by the BF method are shown in Figure 7b.

Also shown in Figure 7 are phase velocities determined by the SASW method (Stokoe *et al.*, 1994; Brown, 1998).

A Rayleigh-wave fundamental mode velocity-dispersion curve calculated from an earth model constructed from borehole logging data and earthquake arrival times is also shown in Figure 7. (V_S of this earth model is shown in Figure 2.)

Measured phase velocities from both HRFK and BF methods are similar at high frequencies and agree with the calculated value to better than 11% above 3.4 Hz. At low frequencies near 2.4 Hz, the HRFK results have smaller error bars and agree more closely with the calculated results.

Figure 8a and 8b show the back azimuth of the highest peak of all the analyzed contour plots by the HRFK and the BF method respectively. There are 31 back-azimuth values at each frequency, corresponding to the 31 separate time segments used in our data analysis. The back azimuths cluster in two groups, one centered around ~145° and the other ~280°. These results are consistent with traffic sources on the Palms to Pines Highway and in the Lake Hemet Campground.

HOLLISTER MUNICIPAL AIRPORT

Site and Array Location

Figure 9 shows the location of two 100-m aperture arrays (Array #1 is to the east of Array #2) and a nearby borehole where velocity logs to a depth of 60 m had been obtained (Gibbs and Fumal, 1994). The borehole is located ~70 m from the northeast tip of Array #2. Figure 10 shows the V_S and geologic logs from the borehole. The sediment consists of clay, sand, gravelly sand, and sandy gravel layers. Kilburn (1972) gives additional geologic information from well logs of four deep oil and gas test holes. (The closest of these four holes, the V. I. Gandrup, O'Connell No.1, is located at ~1.4 km northeast of the 60 m borehole mentioned above; see Figure 9). The unconsolidated or poorly consolidated Tertiary or Quaternary sediment can be grouped into three units. In increasing depth, these are (1) ~310 m of alluvium, old alluvium, San Benito gravel, and alluvial-fan material from the Diablo Range; (2) three or four thick sand sequences separated by thinner clay intervals, totaling ~520 m; and (3) clay, sand, and gravel totaling ~370 m. What is described as consolidated bedrock in the Gandrup well is encountered at ~1160-m depth.

This site is suitable for array measurement of surface waves associated with microtremor in that the traffic sources on the surrounding highways are sufficiently far-off that the microtremor produced by the traffic sources is predominantly surface waves.

Experimental Arrangement

The experimental arrangement is similar to that at the Garner Valley site except that the digital recorder low-pass filter cutoff-frequency was set at 50 Hz.

Microtremor Measurements

Array #1 measurements were conducted from 5:03 p.m., August 31 to 6:24 a.m., September 1, 1995, local time (95:244:00:03 to 95:244:13:24 UTC). In an unsuccessful attempt to extend the measurements to longer periods, the time period was chosen based on a previous site-noise monitoring experiment which determined that microtremor from car and truck traffic decreased markedly after 5 p.m. The microtremor level reached a low between 11 p.m. and 5:30 a.m. (the noise-amplitude ratio between those at 2:30 p.m. and those at midnight is ~11). One factor contributing to the decrease in microtremor is that activities within the uncontrolled airport stopped almost completely after dark and the other factor is the decreased traffic on the highways at night. The first factor implies that, during the array experiment, the microtremor sources were mostly outside the airport. Ground noise was monitored continuously and records were taken at ~60-s segments. Amplifier gain for the geophones was set at 84 dB.

After analyzing the data collected from Array #1, we conducted the second set of array measurements using Array #2 from 3:54 p.m., October 10 to 7:09 a.m., October 11, 1996, local time (96:284:22:54 to 96:285:14:09 UTC). Amplifier gain for the geophones was first set at 78 dB and then changed to 84 dB at 10:23 p.m. The reason for conducting measurements at Array #2 is because of the large difference in phase velocities at 3.9 Hz (~35%) between those determined from Array #1 measurements and those calculated for the fundamental-mode Rayleigh-waves from a plane-layered earth model constructed from the borehole velocity logs (see the Results section). Because Array #1 is located ~350 m away from the borehole, we moved the array location closer to the borehole for the second measurement. The northern tip of Array #2 was located ~70 m from the borehole and our purpose was to find out if phase velocities determined from Array #2 would agree more closely with the calculated Rayleigh-wave velocities.

Data

Figure 11a shows sample microtremor recorded by Array #1 at 3:18 a.m. on September 1, 1995 local time. These records are very similar to each other. Figure 11b shows another set of microtremor recorded by the same array at 3:46 a.m. These records, although less similar to each other, are more representative of the data set. Figure 11c shows microtremor recorded by Array #2 at 6:50 a.m. on October 11, 1996 local time.

7

Data Analysis and Results

We have analyzed our field data using the same procedure as that for the Garner Valley data.

Fourier Spectra. Figure 12 shows the Fourier spectra of the microtremor records shown in Figure 11a. The predominant signals are in the frequency range between 1.8 and 4.5 Hz but there are signals at frequencies as low as 0.5 Hz.

Power-Spectrum Contours. Figure 13a shows the contour plot of $\left|\hat{P}\left(s_x, s_y, \omega\right)\right|$ at 3.91 Hz calculated by the BF method from the microtremor records shown in Figure 11a. Its peak occurs at slowness $s = 2.85\,\text{s}/\text{km}$ with a back azimuth of $\psi = 56°$.

Because the microtremor records in Figure 11a are very similar to each other suggesting that they may be generated by a dominant source, we would like to compare Figure 13a with the contour plot calculated from synthetic microtremor simulating a plane wave of $s = 2.85\,\text{s}/\text{km}$ and $\psi = 56°$ (see Appendix B). As demonstrated by equation (B6), all plane waves traveling with the same slowness vector ($s_x^{(1)}, s_y^{(1)}$) have the same $\hat{P}(s_x, s_y, \omega)$, proportional to a displaced array weight function, regardless of the time variation of the plane waves. Figure 13b shows the theoretical $\left|\hat{P}\left(s_x, s_y, \omega\right)\right|$ contour calculated by the BF method for plane waves with $s = 2.85\,\text{s}/\text{km}$ and $\psi = 56°$. Compare Figure 13b with Figure 13a. There is general agreement between the main lobes down to –6 dB indicating that qualitatively, the observed wavefield is dominated by a single plane surface wave. Compared to the theoretical contours, the observed –3 dB and –6 dB contours of the main lobe are stretched toward the east. The side lobes do not agree as well as the main lobes, with disagreement mainly to the west (the presence of a –6 dB contour in the observation but absent in the theoretical plot).

Figure 13c shows the contour plot $\left|\tilde{P}(s_x, s_y, \omega)\right|$ calculated by the HRFK method from the microtremor records shown in Figure 11a. Its peak occurs at slowness $s = 3.92\,\text{s/km}$ and $\psi = 67°$. It is worthwhile to compare Figure 13a with Figure 13c because the beam pattern is suppressed by the HRFK method in Figure 13c. The peak in Figure 13c occurs further east to that in Figure 13a, consistent with the result that the main lobes in Figure 13a are stretched toward the east relative to the theoretical contours in Figure 13b. In addition, Figure 13c shows that there are two secondary sources of wave energy, one to the northwest and another one to the south. This result is also consistent with the BF contour in Figure 13a which shows a –6 dB side lobe to the west that is absent in the theoretical contour plot of Figure 13b.

We note that slowness determined from the same microtremor data using the two methods differ by ~40% as shown in Figures 13a and 13c. Nevertheless, these two

8

methods yield *statistically* similar results at 3.91 Hz from 35 separate time segments as shown in Figure 15a and 15b.

Figure 14a shows the contour plot of $\left|\hat{P}(s_x, s_y, \omega)\right|$ at 3.91 Hz for beams formed from the less-similar microtremor records shown in Figure 11b; its peak occurs at $s = 1.01$ s/km and $\psi = 139.7°$. Figure 14b shows the theoretical $\left|\hat{P}(s_x, s_y, \omega)\right|$ contour for plane waves with slowness $s = 1.01$ s/km and back azimuth $\psi = 139.7°$. Figures 14a and 14b do not match as well as Figures 13a and 13b. Figure 14c shows that the contour plot $\left|\tilde{P}(s_x, s_y, \omega)\right|$ calculated by the HRFK method from the microtremor records shown in Figure 11b. Because the beam pattern has been suppressed, the broad contours in Figure 14c indicate the presence of multiple sources.

Because the microtremor records shown in Figures 11a and 11b were obtained 28 minutes apart and the experiment conditions at the airport had remained essentially the same, we conclude that differences in the contour plots, Figures 13a and 14a, are caused by changes in the microtremor sources. The different slowness, determined from Figures 13a and 14a ($s = 2.85$ s/km and 1.01 s/km, respectively) indicates that changing source conditions will introduce systematic errors due to interference of power-spectrum contours of multiple waves. We average many measurements in order to reduce the formal standard error of the mean, but this averaging does not remove the systematic errors.

Phase Velocities and Comparison with Rayleigh-Wave Velocities Calculated from Earth Models Constructed from Borehole Logs; Back Azimuths. Phase velocities that are determined by the HRFK method from 35 separate time segments of microtremor records at Array #1 and for frequencies from 1.0 to 3.9 Hz are shown in Figure 15a with five velocity-dispersion curves. The scatter increases at low frequencies because when the wavelength becomes much larger than the array size, measurements become inaccurate for multiple plane waves arriving from different directions (this point will be substantiated later under *Phase Velocities from Synthetic Ground Noise* in THEORETICAL MODELING RESULTS).

Curve #1 is that for Rayleigh waves of the fundamental mode calculated from an earth model constructed using the 60-m deep borehole logging data and a half-space extending downward from the borehole bottom—velocities of the half-space are assumed to be those at the borehole bottom. V_S as a function of depth of this earth model is shown labeled #1 in Figure 16. This relatively flat curve fits poorly to our observation for frequencies < 3 Hz because the low V_S value of 388 m/s, assumed for the half-space, is clearly inappropriate for the entire sedimentary sequence from 60 m to ~1160 m.

Curve #2 is calculated using an earth model constructed from the borehole logs for the top 60 meters and estimated for the lower depths to 1160 m guided by the geologic

information from Kilburn (1972). Extrapolations for V_S from 60 m to 1160 m are based on the equation,

$$V_S = V_{S0}(z/z_0)^{0.25}.$$

(1)

By choosing $V_{S0} = 400$ m/s at $z_0 = 60$ m, we obtain a subjectively chosen lower bound consistent with the measured velocities in the top 60-m. The continuous model from equation (1) is then used to construct a constant-velocity-layered model under the condition that the layered and continuous models yield the same travel time across each layer. Velocity of the bottom layer is also assumed for the bedrock below 1160-m. (See the model #2 in Figure 16.) We obtain curve #3 by using the more appropriate bedrock velocities [$V_S = 2.0$ km/s and $V_P = 4.0$ km/s, guided by Yamamizu and Goto, (1978) and Yamamizu et al. (1981)] in the earth model for curve #2. (See model #3 in Figure 16.)

Curves #4 and #5 are calculated when the V_S estimation for unconsolidated or poorly consolidated materials from 60 m to 1160 m is a subjectively chosen upper bound consistent with the measured velocities in the top 60 m [using $V_{S0} = 600$ m/s at $z_0 = 60$ m in equation (1)]. Velocity of the material at 1160 m is assumed for the bedrock in the model for curve #4 whereas $V_S = 2.0$ km/s and $V_P = 4.0$ km/s were used as bedrock velocities for curve #5. (See models #4 and #5 in Figure 16.)

In Figure 15a the calculated phase velocities at 3.9 Hz from all models, however, are essentially the same (indicating that phase velocity is not influenced significantly by layers deeper than 60 m) and are lower than the measured phase velocity by ~35%. Curves #2, #3, #4, and #5 show that the bedrock is sufficiently deep that the bedrock velocities have negligible effects on phase velocities for frequencies $\geq$ 1 Hz.

Figure 15b shows the phase velocities from the same 35 segments of microtremor records at Array #1 as determined by the BF method. Comparing the results in Figures 15a and 15b, the mean values agree closely with each other from 2.20 to 3.91 Hz. Below 2.20 Hz, the mean phase velocities from the HRFK method fall between dispersion curves #3 and #5, whereas 4 out of 5 values from the BF method lie above the dispersion curve #5. The two methods give overlapping error bars for the measurements but non-overlapping error bars for the mean.

Phase velocities determined from 67 segments of microtremor records at Array #2 determined by the HRFK method are shown in Figure 17a. The agreement between the measured and the calculated phase velocity at 3.91 Hz is much closer than that for the Array #1 data, an encouraging result because, in contrast to Array #1, one tip of Array #2 is only 70 m away from the borehole. Figure 17b shows the phase velocities from the same 67 segments of microtremor records but determined by the BF method. Comparing the results in Figures 17a and 17b, the mean values agree closely with each other from 2.93 to 3.91 Hz. Below 2.93 Hz, the mean phase velocities from the HRFK method fall

between dispersion curves #3 and #5 whereas those determined from the BF method increase with decreasing frequency and rise above dispersion curve #5 below 2.2 Hz. Again, the two methods give overlapping error bars for the measurements but non-overlapping error bars for the mean.

Figure 18a shows the back azimuth of the peak in the measured power-spectral contour plots for Array #1 by the BF method. Figure 18b shows the back azimuth of the peak in the measured power-spectral contour plots for Array #2 by the BF method. There is increased back-azimuth distribution between ~45° and ~225° for both plots. Back azimuths from the HRFK method show similar results.

DISCUSSION AND CONCLUSIONS

We have measured the phase velocities of surface waves associated with microtremor at two California sites using surface arrays.

In order to compare a V_S depth profile from borehole methods with our phase-velocity results, we calculate the fundamental-mode Rayleigh-wave phase velocities from an earth model constructed from the borehole data. The alternative comparison by inverting our phase-velocity results to obtain a V_S depth profile involves additional uncertainties introduced by the inversion process.

The simpler geologic conditions at Garner Valley and a velocity structure determined by borehole methods to 500-m in granite allow a meaningful comparison of measured phase velocities with the dispersion curve calculated from the velocity structure. We found that observations agree with borehole results to better than 11% except when the wavelength is >2 times the array aperture, in which case the observations have increased scatter and biased high relative to the dispersion curve. Simulations show that at wavelengths >2 times the array aperture the phase velocities calculated from multiple waves arriving from different azimuths may deviate by large amounts from the correct value. (See Appendix B: Theoretical Modeling Results.)

At Hollister Airport, where we have velocity data only to 60-m depth, the phase velocity at 3.9 Hz (near the upper edge of the microtremor frequency band) is not influenced significantly by layers deeper than 60 m. The phase velocity measured by a 100-m array ·70 m from the borehole is within 20% of the calculated Rayleigh-wave velocity. At lower frequencies, the measured phase velocities from the HRFK method generally fall within the dispersion curves calculated using the estimated lower and upper bounds of the velocity profile. On the other hand, phase velocities determined from the BF method increase with decreasing frequency and rise above the upper bounds of the velocity profile below 2.2 Hz.

Compared to surface methods using controlled sources and explosions, the present method is convenient in that no source is required from the experimenter. For correct

11

results, however, the microtremor sources, usually highway traffic, must be located sufficiently far away that the motion at the array is predominantly surface waves. Because microtremor is time- and site-dependent, in some places the frequency band of ground noise may not cover the frequencies of interest. Figure 19 shows the difference in microtremor spectra at the two sites of this study. The difference in frequency content of the ground noise has an impact on the depths to which shear-wave velocities can be determined: ground noise in a limited frequency band, as shown in Figure 19, results in limited resolution of shear-wave velocities both at shallow depths and at deeper depths. A practical example of the limited depth resolution implied by the differences in spectral content shown in Figure 19 is the determination of the average shear-wave velocity in the upper 30 m (which we term "V30"), used in the NEHRP Provisions (NEHRP 1997) and the 1997 Uniform Building Code (ICBO 1997). Brown et al. (2000) suggested that V30 correlates well with the fundamental-mode Rayleigh wave phase velocity of 40-m wavelength. At the Garner Valley site, our measured phase velocity at the highest frequency available (5.9 Hz) equals 257 m/s, implying a wavelength of 44 m; we therefore expect that the measured dispersion data can be used to obtain a good estimate of V30. In contrast, at Hollister Array #2, the wavelength of the highest available frequency (3.9 Hz) equals 84 m, which indicates that the frequencies are too low to obtain a good estimate of V30. In this case, however, active source could be used to obtain phase velocities at higher frequencies.

Because shear-wave velocity is the predominant factor controlling Rayleigh-wave phase velocities, surface-wave methods can provide V_S information adequate for ground motion estimation. The agreement of results from this non-intrusive method and those obtained from borehole measurements, particularly at Garner Valley, gives us confidence in the microtremor method for ground motion estimation and site characterization when the following two conditions are met. The first condition is that the site velocity structure approximates a horizontally layered structure at least on the size of the seismic array. This condition is required because the present method of array data analysis assumes a laterally homogeneous velocity structure. The second condition, based on numerical simulations in Appendix B, requires that the surface wavelength is <~2 times of the array aperture.

ACKNOWLEDGMENTS

programs (Herrmann, 1996); and Drs. Jon B. Fletcher, Arthur F. McGarr, Ken Miyakoshi, Jose M. Roesset, and James C. Savage, whose reviews improved our manuscript. This work is performed as a cooperative project between the U.S. Geological Survey and the U.S. Nuclear Regulatory Commission.

REFERENCES

Aki, K. and P. G. Richards (1980). *Quantitative Seismology*, W. H. Freeman and Co., San Francisco, California.

Asten, M. W. (1977). Theory and practice of geophone calibration in situ using a modified step method, *IEEE Trans. Geosci. Electron.*, **GE-15**, 208–214.

Boore, D. M., W. B. Joyner, and T. E. Fumal (1997). Equations for estimating horizontal response spectra and peak acceleration from Western North American earthquakes: a summary of recent work, *Seism. Res. Lett.*, **68**, 128–153.

Borcherdt, R. D., J. B. Fletcher, E. G. Jensen, G. L. Maxwell, J. R. VanSchaack, R. E. Warrick, E. Cranswick, M. J. S. Johnston, and R. McClearn (1985). A general earthquake-observation system (GEOS), *Bull. Seism. Soc. Am.*, **75**, 1783–1825.

Brown, L. T. (1998). Comparison of V_S profiles from *SASW* and borehole measurements at strong motion sites in southern California: M. S. thesis, University of Texas, Austin, 349 p.

Brown, L. T., D. M. Boore, and K. H. Stokoe, II (2000). Comparison of shear wave velocity profiles from SASW and downhole seismic tests at a strong-motion site, Proc. *12th World Conference on Earthquake Engineering, Auckland, New Zealand, 30 January – 4 February, 2000,* in press.

Brown, L. T., J. G. Diehl, and R. L. Nigbor (2000). A simplified procedure to measure average shear-wave velocity to a depth of 30 meters (VS30) using surface waves, *Seism. Res. Lett.*, **71**, 249.

Capon, J. (1969). High-resolution frequency-wavenumber spectrum analysis, *Proc. IEEE*, **57**, 1408–1418.

Capon, J. (1973). Signal processing and frequency-wavenumber spectrum analysis for a large aperture seismic array, in *Methods in Computational Physics*, **13**, *Geophysics*, B. A. Bolt, ed., Academic Press, New York, New York, 1–59.

Capon, J., R. J. Greenfield, and R. J. Kolker (1967). Multidimensional maximum-likelihood processing of a large aperture seismic array, *Proc. IEEE*, **55**, 192–211.

Charlie, W. A., G. T. Jirak, and D. O. Doehring (1985). Seismic analysis of Horse Creek Dam, Hudson, Colorado, Proc. *Conf. on Measurement and Use of Shear Wave Velocity for Evaluating Dynamic Soil Properties, Denver, Colorado, May 1, 1985*, R. D. Woods, ed., American Society of Civil Engineers, New York, New York.

Gibbs, J. F. and T. E. Fumal (1994). Seismic velocities and velocity logs from borehole measurements at seven strong-motion stations that recorded the 1989 Loma Prieta, California, Earthquake, Part IV, *U. S. Geol. Surv. Open-File Rep. 94–552*.

Graves, R. W. (1998). Three-dimensional finite-difference modeling of the San Andreas Fault: source parameterization and ground-motion levels, *Bull. Seism. Soc. Am.,* **88**, 881–897.

Herrmann, R. B. (1996). *Computer Programs in Seismology: 3.0*, Saint Louis University, Saint Louis, Missouri.

Horike, M. (1985). Inversion of phase velocity of long-period microtremor to the S-wave-velocity structure down to the basement in urbanized areas, *J. Phys. Earth,* **33**, 59–96.

ICBO (1997). *1997 Uniform Building Code, Vol. 2*, International Conference of Building Officials, Whittier, California.

Kawase, H., T. Satoh, T. Iwata, and K. Irikura (1998). S-wave velocity structure in the San Fernando and Santa Monica areas, *The Effects of Surface Geology on Seismic Motion*, K. Irikura, K. Kudo, H. Okada, and T. Sasatani, eds., A. A. Balkema, Rotterdam, 733–740.

Kilburn, C. (1972). Ground-water hydrology of the Hollister and San Juan Valleys, San Benito County, California, 1913–1968, *U. S. Geol. Surv. Open-File Rep. 73–0144*, 9–13.

Kramer, S. L. (1996). *Geotechnical Earthquake Engineering*, Prentice-Hall, Upper Saddle River, New Jersey.

Lacoss, R. T., E. J. Kelly, and M. N. Toksöz (1969). Estimation of seismic noise structure using arrays, *Geophysics,* **34**, 21–38.

Liu, H.-P. and L. Peselnick (1986). Improved phase-ellipse method for in situ geophone calibration, *Geophys. Prospect.,* **34**, 537–544.

Liaw, A. L. (1977). Microseisms in geothermal exploration: Studies in Grass Valley, Nevada: Ph.D. thesis, University of California, Berkeley, 168 p.

Malagnini, L., R. B. Herrmann, A. Mercuri, S. Opice, G. Biella, and R. de Franco (1997). Shear-wave velocity structure of sediments from the inversion of explosion-

14

induced Rayleigh waves: comparison with cross-hole measurements, Bull. *Seism. Soc. Am.*, **87**, 1413–1421.

Milana, G., S. Barba, E. Del Pezzo, and E. Zambonelli (1996). Site response from ambient noise measurements: new perspective from an array study in Central Italy, *Bull. Seism. Soc. Am.*, **86**, 320–328.

NEHRP (1997). *NEHRP Recommended Provisions for Seismic Regulations for New Buildings and Other Structures, Part 1: Provisions*, Building Seismic Safety Council, Washington, D. C.

Oppenheimer, D. H., and H. M. Iyer (1980). Frequency-wavenumber analysis of geothermal microseisms at Norris Geyser basin, Yellowstone National Park, Wyoming, *Geophysics*, **45**, 952–963.

Steidl, J. H., A. G. Turmarkin, and R. J. Archuleta (1996). What is a reference site? *Bull. Seism. Soc. Am.*, **86**, 1733–1748.

Stokoe, II, K. H., and S. Nazarian (1985). Use of Rayleigh waves in liquefaction studies, Proc. *Conf. on Measurement and Use of Shear Wave Velocity for Evaluating Dynamic Soil Properties, Denver, Colorado, May 1, 1985*, R. D. Woods, ed., American Society of Civil Engineers, New York, New York.

Stokoe, II, K. H., S. G. Wright, J. A. Bay, and J. M. Roesset (1994). Characterization of geotechnical sites by SASW method, *Geophysical Characterization of Sites*, R. D. Woods, ed., A. A. Balkema, Rotterdam, 15–25.

Yamamizu, F., and N. Goto (1978). Direct measurement of seismic wave velocities in deep soil deposits, Proc. *5th Japan Earthquake Engineering Symposium*, 329–336.

Yamamizu, F., H. Takahashi, N. Goto, and Y. Ohta (1981). Shear wave velocities in deep soil deposits. Part III — Measurements in the borehole of the Fuchu Observatory to the depth of 2,750 m and a summary of the results, *ZISIN, J. of the Seism. Soc. of Japan*, 465–479.

APPENDIX A: SUMMARY OF DATA-ANALYSIS METHODS

The Frequency-Wavenumber Power-Spectrum or Beam-Forming Method

This method estimates the wavefield power-spectrum by the process of beam forming (Aki and Richards, p. 619–623, 1980):

Expressing the microtremor time-series recorded at the station j with coordinates (x_j, y_j) as $n_j(t)$, the beam output is

15

$$b(s_x, s_y, t) = \frac{1}{K} \sum_{j=1}^{K} n_j(t + t_j),$$ (A1)

where K is the number of array stations ($K = 10$ for our arrays) and

$$t_j = s_x(x_j - x_1) + s_y(y_j - y_1), \qquad j = 1, 2, ..., 10,$$ (A2)

are station time shifts; (s_x, s_y) is the slowness vector. The power-spectrum of $b(s_x, s_y, t)$, $\hat{P}(s_x, s_y, \omega)$, is given by the Fourier transform [using the sign convention of Aki and Richards (1980), p. 130] of its auto-correlation,

$$\hat{P}(s_x, s_y, \omega) = \int \exp(i\omega\tau) \frac{1}{K^2} \langle \sum_{j=1}^{K} n_j(t + t_j) \sum_{l=1}^{K} n_l(t + t_l + \tau) \rangle d\tau.$$ (A3)

where $\langle \ \rangle$ designate average over t. $\hat{P}(s_x, s_y, \omega)$ is a weighted average of the true frequency-slowness power-spectrum $P(s_x, s_y, \omega)$ of the wavefield, i.e.,

$$\hat{P}(s_x, s_y, \omega) = \int_{-\infty}^{\infty} \int_{-\infty}^{\infty} W(\sigma_x - s_x, \sigma_y - s_y, \omega) P(\sigma_x, \sigma_y, \omega) d\sigma_x d\sigma_y,$$ (A4)

where the weight function $W(s_x, s_y, \omega)$, given by

$$W(s_x, s_y, \omega) = \frac{1}{(2\pi K)^2} \sum_{j,l=1}^{K} \exp\left\{-i\omega\left[s_x(x_j - x_l) + s_y(y_j - y_l)\right]\right\},$$ (A5)

depends only on the slowness vector (s_x, s_y), the angular frequency ω, and the array configuration defined by $\{(x_j, y_j), \ j = 1, 2, ..., K\}$. The maximum of $|W(s_x, s_y, \omega)|$ occurs at $s_x = s_y = 0$ and equals $1/(4\pi^2)$.

For a particular frequency, the magnitude of $\hat{P}(s_x, s_y, \omega)$ calculated by equation (A3) can be plotted as a function of s_x and s_y; the distance in the s_x-s_y plane from the origin to the peak location gives the experimentally determined slowness of the dominant surface wave. In computations using equation (A3), we replace the time-average by a sample-average: each microtremor record of 8192 samples (40.96 s long) is divided into nine staggered records each of 4096 samples with an overlap of 3584 sample points (Figure A1). Nine power spectra, calculated from the nine record sections, are averaged to yield the power-spectrum estimate, equation (A3).

16

This method calculates the power output, $\tilde{P}(s_x, s_y, \omega)$, of a maximum-likelihood array processor filter by

$$\tilde{P}(s_x, s_y, \omega) = \frac{1}{M} \sum_{n=1}^{M} \left| \sum_{j=1}^{K} A_j^*(s_x, s_y, \omega) S_{jn}(\omega) \exp[i\omega(s_x x_j + s_y y_j)] \right|^2 ; \qquad (A6)$$

where " * " means complex conjugate, the summation n is over the M record sections and the summation j is over the K array stations. In equation (A6),

$$A_j(s_x, s_y, \omega) = \frac{\sum_{l=1}^{K} q_{jl}(s_x, s_y, \omega)}{\sum_{j,l=1}^{K} q_{jl}(s_x, s_y, \omega)}, \qquad (A7)$$

where the matrix $\left\{ q_{jl}(s_x, s_y, \omega) \right\}$ is the inverse matrix of $\left\{ \hat{f}_{jl}(\omega) \exp[i\omega s_x(x_j - x_l) + i\omega s_y(y_j - y_l)] \right\}$. The spectral matrix $\left\{ \hat{f}_{jl}(\omega) \right\}$ is given by

$$\hat{f}_{jl}(\omega) = \frac{1}{M} \sum_{n=1}^{M} S_{jn}(\omega) S_{ln}^*(\omega) \qquad j,l = 1,\ldots,K, \qquad (A8)$$

where $S_{jn}(\omega)$ is the Fourier transform of the data in the n-th record section of the j-th station.

The main advantage of the HRFK method over the BF method is its ability to suppress the side lobes. However, its application is restricted to the case $M \geq K$ unless a small amount of incoherent noise is added to the array data. For the HRFK method, we used $M = 17$ overlapping record sections ($K = 10$ stations), 4096 samples per record section, and 256 samples offset between successive record sections.

APPENDIX B: THEORETICAL MODELING RESULTS

We gain insight into our experimental results by modeling using synthetic ground noise. We generate synthetic plane surface waves from a single direction as follows: A uniformly distributed random-number generator first produces a time-series $g(t)$; let $G(\omega) = F[g(t)]$. The synthetic ground noise at station j is given by

$$n_j(t) = F^{-1}\left\{ G(\omega) L(\omega) \exp[i\omega(s_x^{(1)} x_j + s_y^{(1)} y_j)] \right\}, \qquad j = 1,2,\ldots,10, \qquad (B1)$$

where F and F^{-1} denote Fourier and inverse Fourier transforms, $L(\omega)$ is a low-pass filter, and $(s_x^{(1)}, s_y^{(1)})$ is an assigned slowness vector.

Synthetic ground noise simulating time-uncorrelated plane surface waves coming from two directions are given by

$$n_j(t) = \frac{w^{(1)}}{2\pi} \int_{-\infty}^{\infty} G^{(1)}(\omega)\, L(\omega) \exp\left[i\omega\left(s_x^{(1)} x_j + s_y^{(1)} y_j - t\right)\right] d\omega +$$

$$\frac{w^{(2)}}{2\pi} \int_{-\infty}^{\infty} G^{(2)}(\omega) L(\omega) \exp\left[i\omega\left(s_x^{(2)} x_j + s_y^{(2)} y_j - t\right)\right] d\omega, \quad j = 1, 2, \dots, 10, \text{ (B2)}$$

where $g^{(1)}(t)$ and $g^{(2)}(t)$ are two independent random time-series, $G^{(1)}(\omega) = F[g^{(1)}(t)]$, $G^{(2)}(\omega) = F[g^{(2)}(t)]$, $(s_x^{(1)}, s_y^{(1)})$ and $(s_x^{(2)}, s_y^{(2)})$ are assigned slowness vectors, and $w^{(1)}$ and $w^{(2)}$ are weighing factors with $w^{(1)} + w^{(2)} = 1$. Multiple plane surface waves coming from more than two directions can be generalized from equation (B2).

Incoherent noise specific to each station can be added to the synthetic ground noise, equation (B1) or equation (B2), by adding a term,

$$\frac{r_j}{2\pi} \int_{-\infty}^{\infty} \Phi_j(\omega) L(\omega) \exp(-i\omega t)\, d\omega, \quad\quad\quad \text{(B3)}$$

to $n_j(t)$, $j = 1, 2, \dots, 10$, where $\phi_1(t), \phi_2(t), \dots, \phi_{10}(t)$ are independent random time-series, $\Phi_j(\omega) = F[\phi_j(t)]$, and $r_1, r_2, \dots, r_{10}$ are scaling constants.

Results obtained from synthetic ground noise are given below.

$\hat{P}(s_x, s_y, \omega)$ of Plane Waves Traveling with Slowness $(s_x^{(1)}, s_y^{(1)})$

The frequency-slowness power-spectrum $P(s_x, s_y, \omega)$ of a plane surface wave coming from a single direction,

$$n(x, y, t) = \frac{1}{2\pi} \int_{-\infty}^{\infty} N(\Omega) \exp\left[i\Omega\left(s_x^{(1)} x + s_y^{(1)} y - t\right)\right] d\Omega, \quad\quad\quad \text{(B4)}$$

where $(s_x^{(1)}, s_y^{(1)})$ is the slowness vector of the plane-wave, is given by

$$P(s_x, s_y, \omega) = 2\pi \frac{|N(\omega)|^2}{\omega^2} \delta\left(s_x - s_x^{(1)}\right) \delta\left(s_y - s_y^{(1)}\right), \tag{B5}$$

Where $\delta(s)$ is the Dirac delta function. Substitute equation (B5) into equation (A4),

$$\hat{P}(s_x, s_y, \omega) = 2\pi \frac{|N(\omega)|^2}{\omega^2} W\left(s_x^{(1)} - s_x, s_y^{(1)} - s_y, \omega\right), \tag{B6}$$

i.e., for a wavefield characterized by a single plane surface wave, the power-spectrum of the output-beam formed from the array microtremor records is proportional to the array weight function with its origin in the s_x-s_y plane shifted to $\left(s_x^{(1)}, s_y^{(1)}\right)$.

While analyzing the field data, we can compare our experimentally determined contour plot of $\left|\hat{P}(s_x, s_y, \omega)\right|$ with that of $\left|\hat{P}(s_x, s_y, \omega)\right|$ calculated from equation (B6). If the experimentally determined contour plot matches closely with that of the theoretical contour plot, we can state qualitatively that the observed wavefield is dominated by a single plane surface wave (see Figures 13a and 13b).

Phase Velocities from Simulated Array Measurements of Synthetic Ground Noise

Effect of Single Source. We first model the case for a single plane wave. Figure B1 shows the sample results. The array configuration is that of the Garner-Valley array. Circles are mean values of phase velocities from field measurements and the solid curve is the dispersion curve calculated from an earth model. The synthetic ground noise simulates a plane wave traveling at the calculated phase velocity (solid curve) at the indicated frequency and from a given back azimuth (indicated on top of each figure); a incoherent noise time series specific to each array element ($S / N = 10$) has been added to each microtremor. (Possible sources of incoherent noise are small animals and wind. Because the wind was dying down when the data were obtained, it is likely that such incoherent noise were small. On the other hand, the traffic on the surrounding highways, our coherent noise sources, continued throughout the night.) The stars are phase velocities from power-spectral calculation (using the HRFK method) of the synthetic ground noise. The results show that when the wavelength is 8.5 times the array size (at 1.7 Hz), the phase velocity of a single incoming wave in the presence of local noise can be measured to an accuracy of 3.7% (top figure), 2.0% (middle figure), and 17.5% (bottom figure), respectively.

Effect of Multiple Sources. The situation is significantly different when there are two incoming plane waves traveling with the same slowness but from different back azimuths. Sample results obtained by the HRFK method for the configuration of the Garner-Valley array are shown in Figure B2. Power-spectrum contours are shown in Figure B3 (for the case Azimuths = 145° and 260°. At wavelengths > 1.8 times the array

aperture (at 3.2 Hz), phase velocity from the power-spectral calculations may deviate by a large amount from the phase velocity of the plane waves; the calculated phase velocity is generally biased to a higher value in the bottom two figures. The increase in phase-velocity scatter from synthetic ground noise at low frequencies in Figure B2 is similar to those from the observational results in Figure 7.

SCALE 1:24 000

CONTOUR INTERVAL 40 FEET
NATIONAL GEODETIC VERTICAL DATUM OF 1929
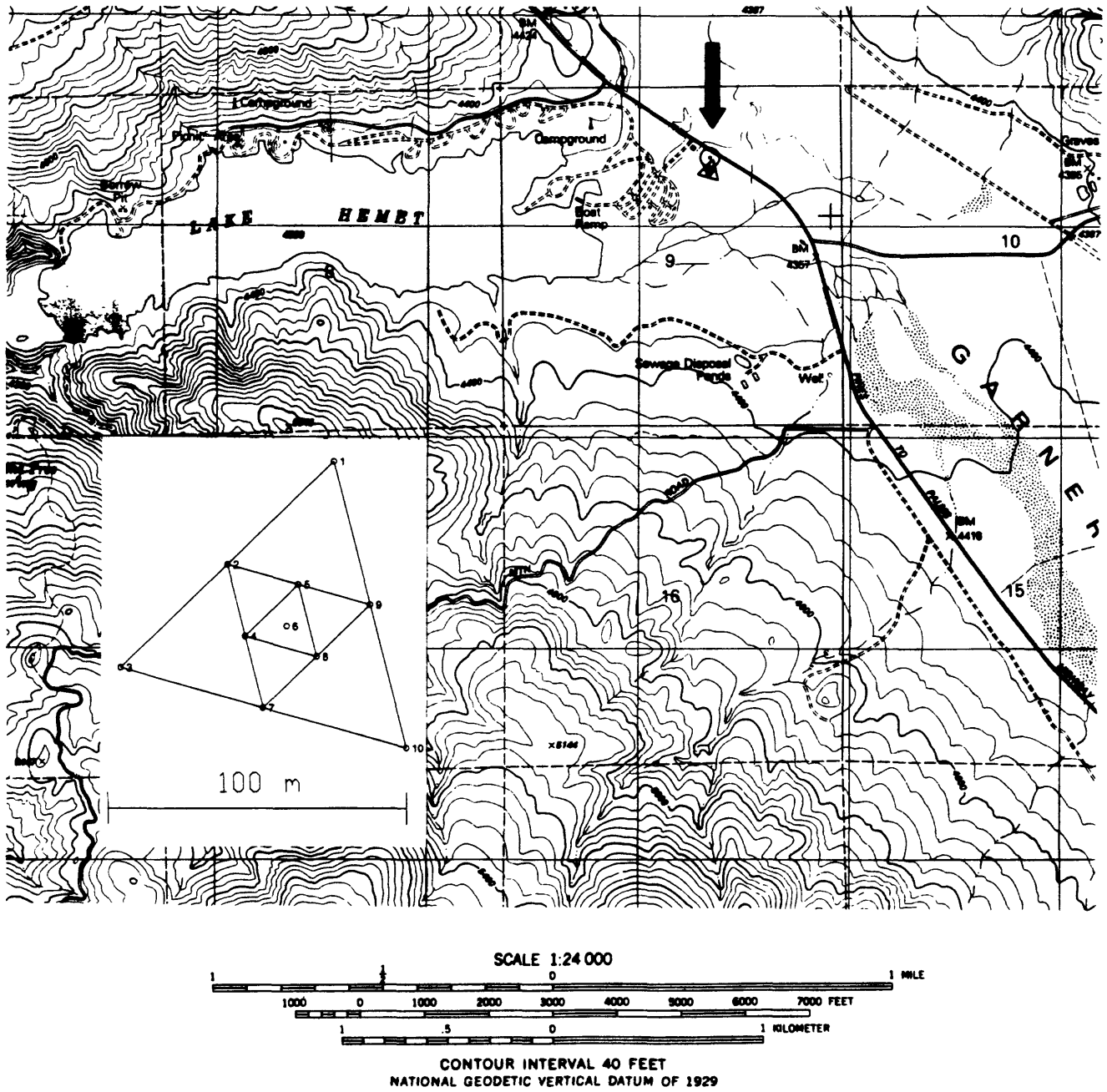
Figure 1. Array location at the Garner Valley site; an arrow points to the 100-m aperture array and a dot in a circle locates the 500-m deep borehole. The array configuration is shown in the insert.
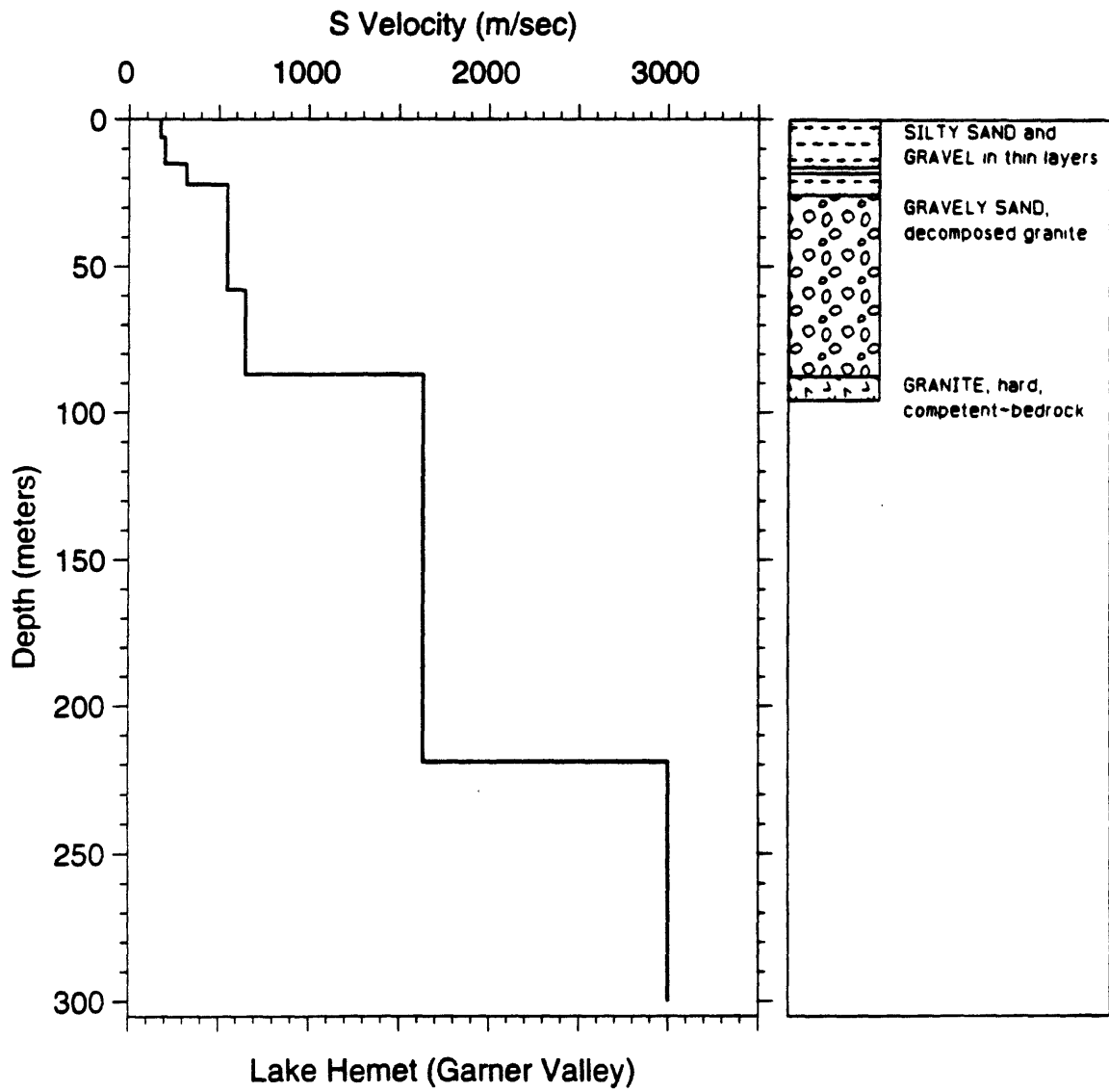
Figure 2. Shear-wave velocities and simplified geologic log of the Garner Valley site.
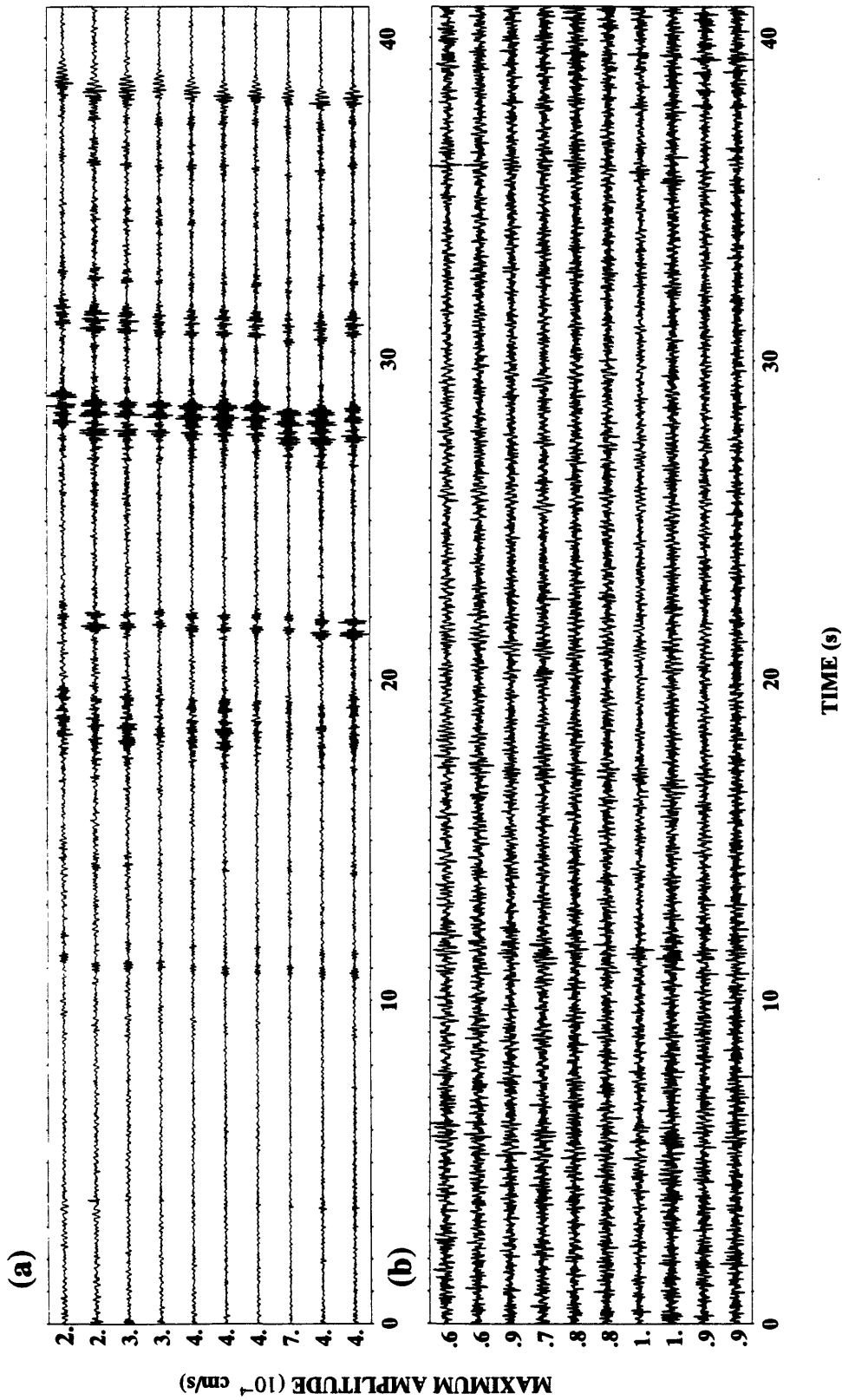
Figure 3. Microtremor recorded by the Garner-Valley array; (a) these records are very similar to each other. In contrast, records in (b) are less similar to each other.

23
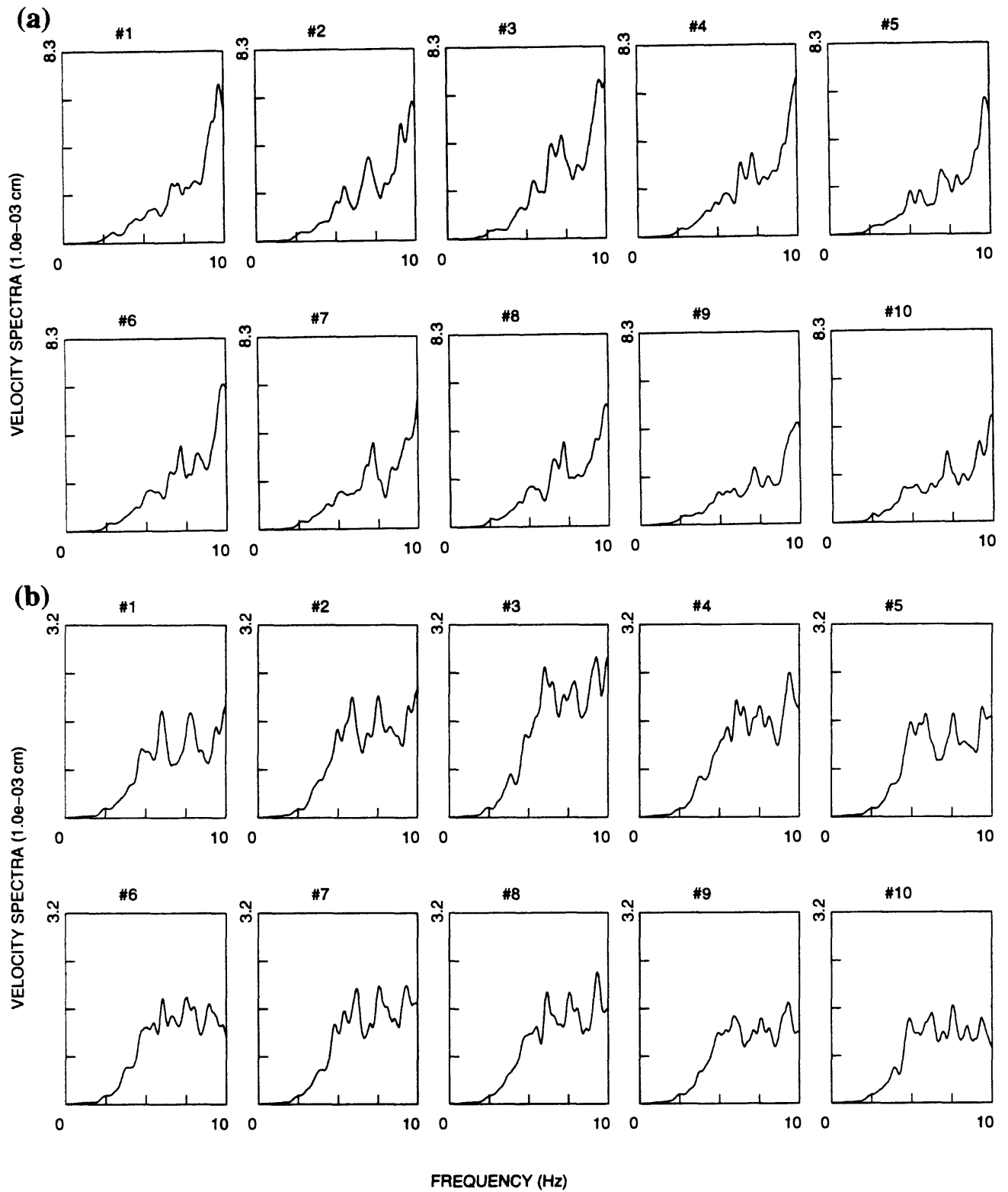
Figure 4. (a) Fourier spectra of the microtremor records obtained by the Garner-Valley array shown in Figure 3a, and (b) Fourier spectra of the microtremor records shown in Figure 3b.

24
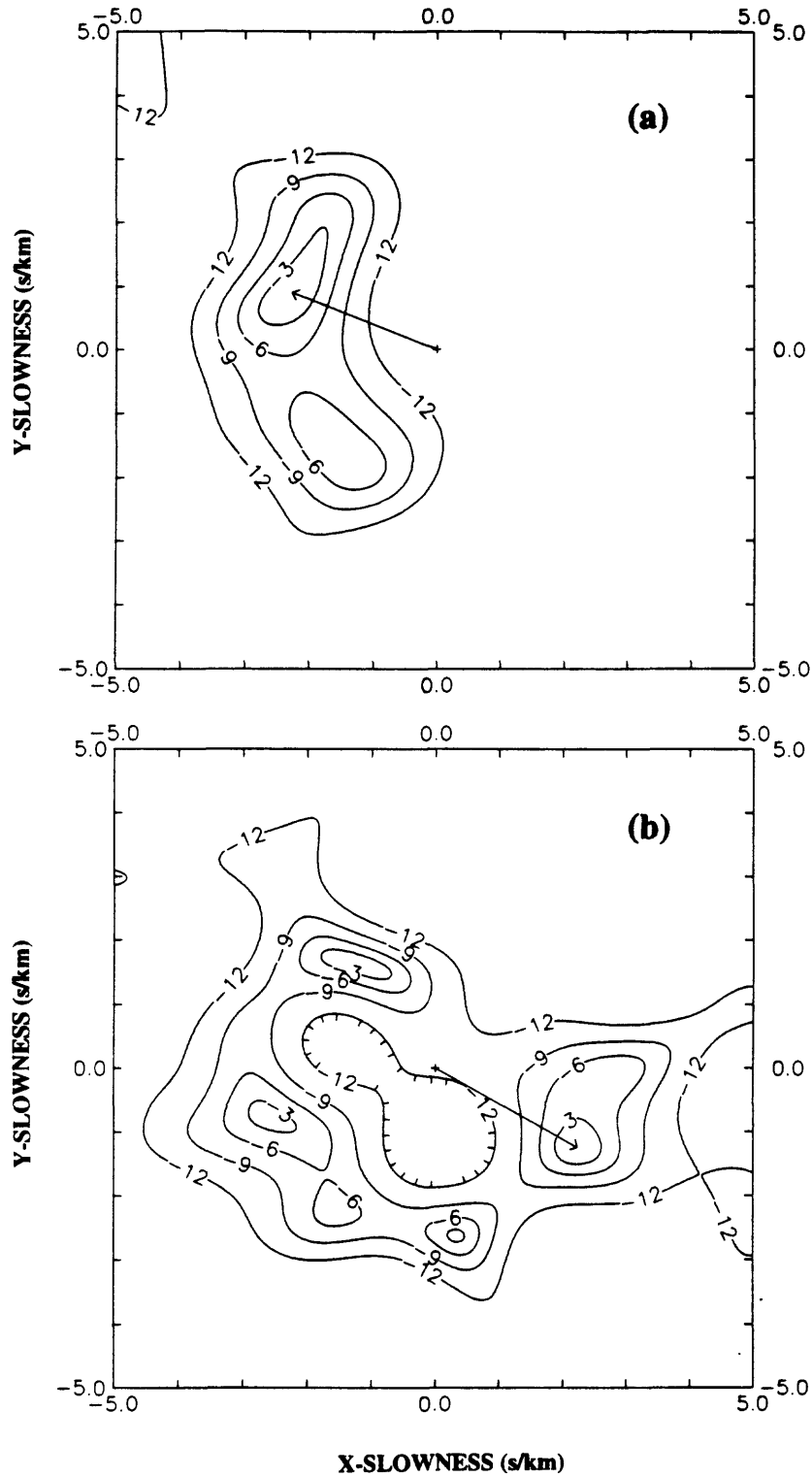
Figure 5. (a) Contour plot of $\left|\tilde{P}(s_x, s_y, \omega)\right|$ by the HRFK method at 4.6 Hz for microtremor records shown in Figure 3a. Two contour peaks are resolved with the highest peak at a back azimuth of 291.5°. (b) Contour plot of $\left|\tilde{P}(s_x, s_y, \omega)\right|$ at 4.6 Hz for microtremor records shown in Figure 3b. In contrast to (a), five resolved peaks are displayed.
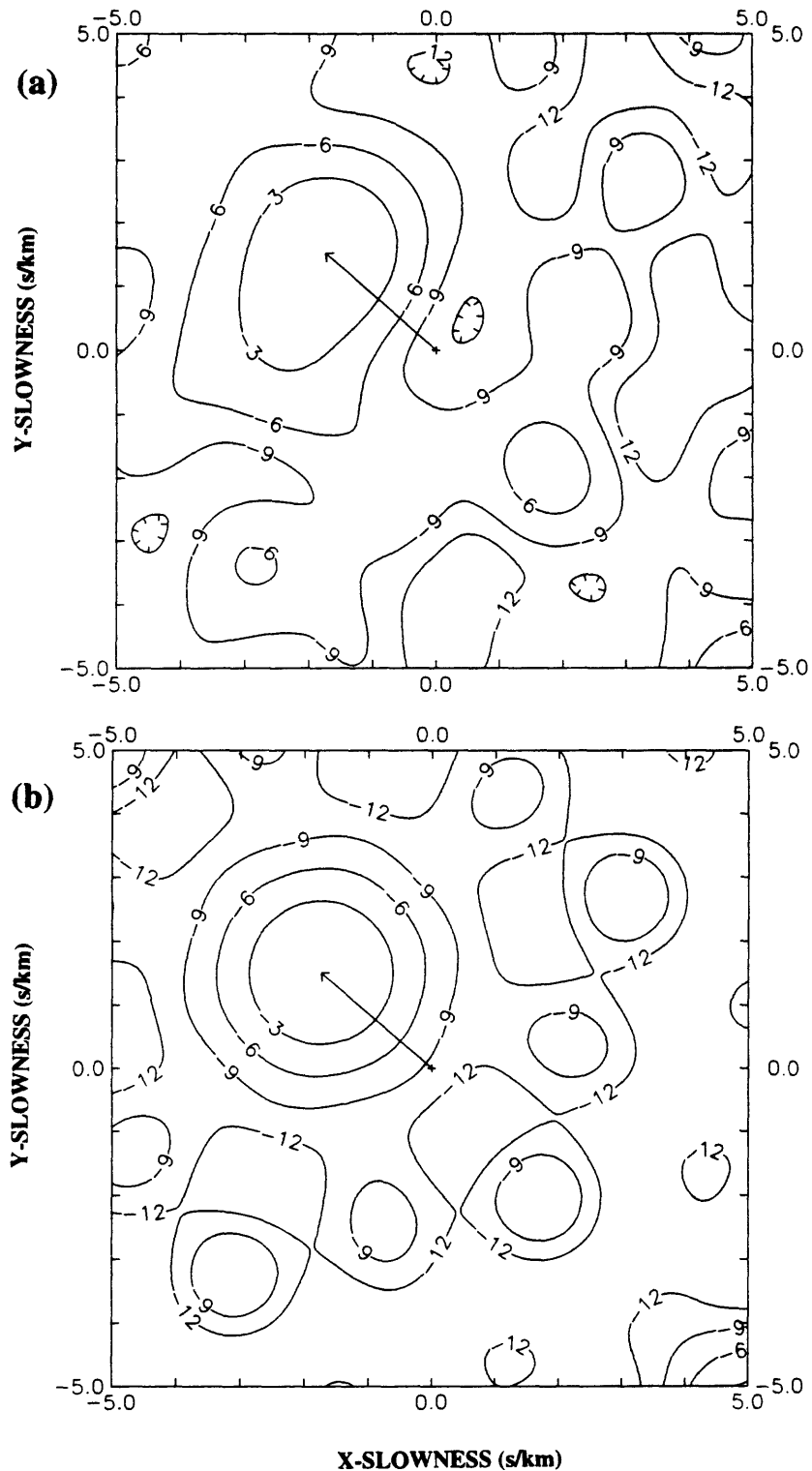
Figure 6. (a) Contour plot of $\left|\hat{P}(s_x, s_y, \omega)\right|$ by the BF method at 4.6 Hz for microtremor records shown in Figure 3a. In contrast to two resolved peaks by the HRFK method in Figure 5a, there is one broad peak at a slowness of $s = 2.29$ s/km and a back azimuth of 310.9°. (b) Theoretical contour plot of $\left|\hat{P}(s_x, s_y, \omega)\right|$ at 4.6 Hz for plane waves with slowness $s = 2.29$ s/km and back azimuth $\psi = 310.9°$.
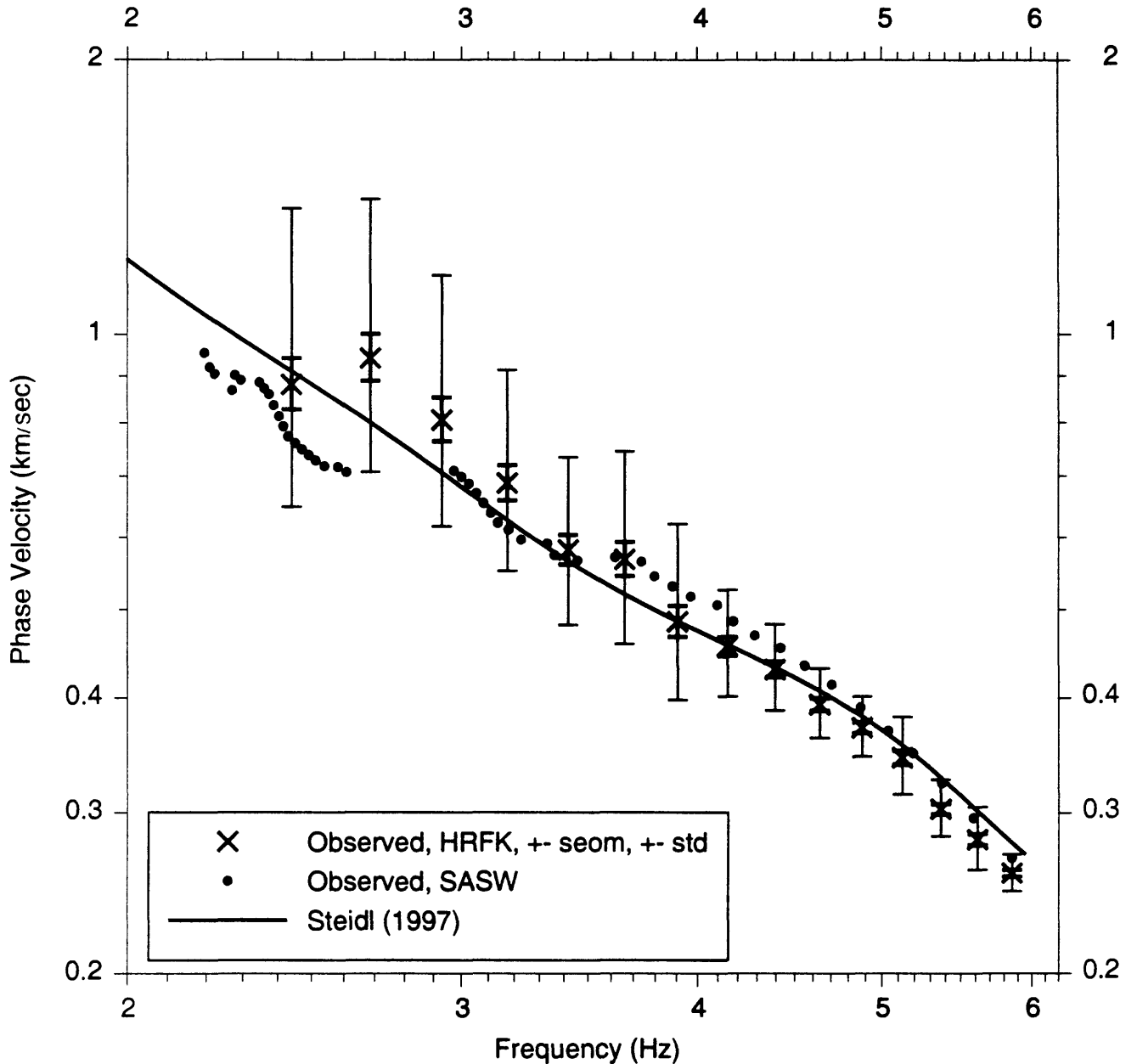
Figure 7a. Phase velocities obtained from 31 separate time segments of the Garner-Valley array using the high-resolution-frequency-wavenumber (HRFK) spectrum-analysis method and a velocity-dispersion curve calculated from an earth model (Steidl, 1997). Light error bar represents ± 1 standard deviation (std) of the phase velocity; heavy error bar represents ± 1 standard error of the mean (seom). Phase velocities obtained at the same site by the SASW method (Brown, 1998) are also included for comparison.
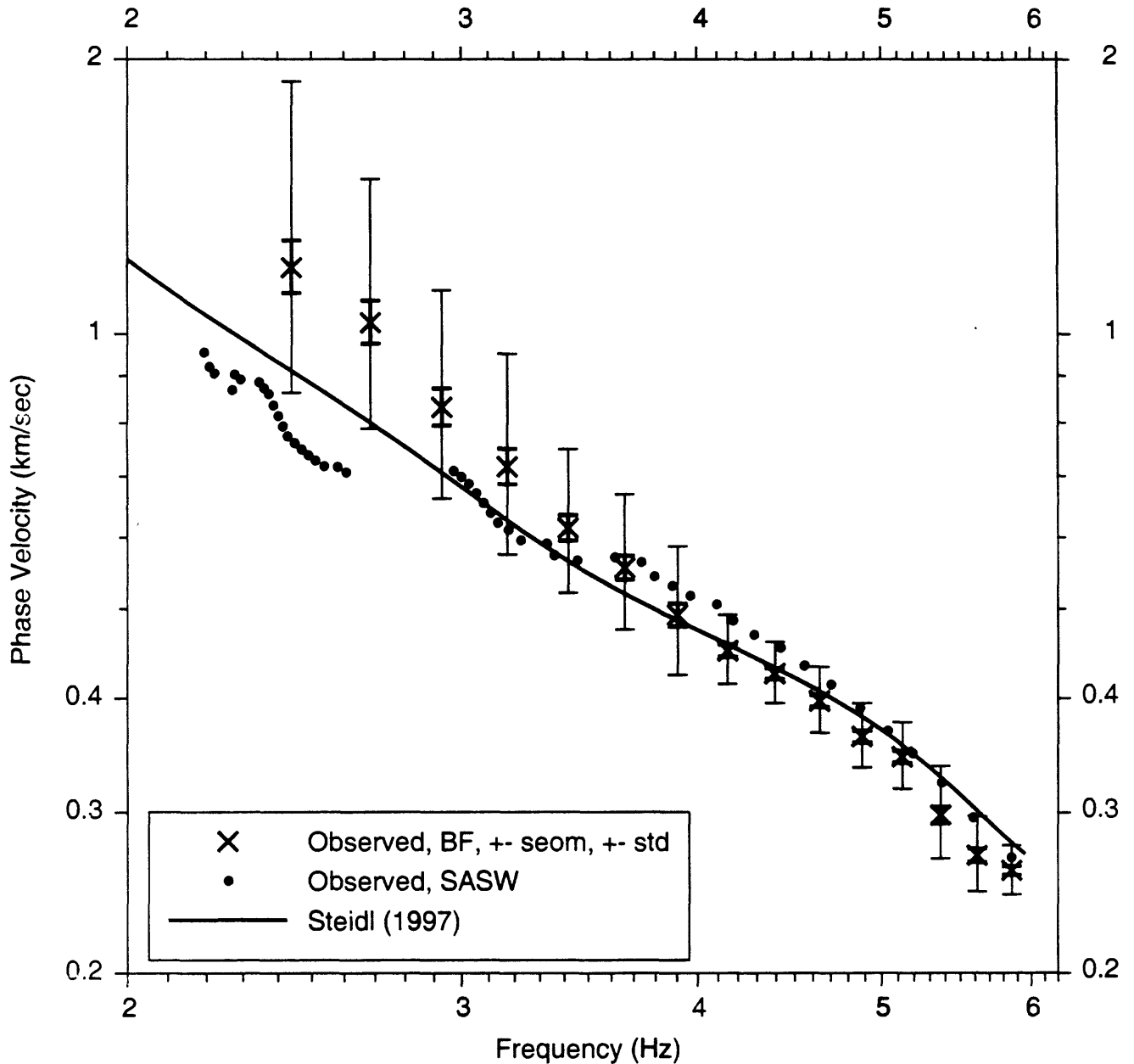
Figure 7b. Phase velocities obtained from 31 separate time segments of the Garner-Valley array using the beam-forming (BF) method and a velocity-dispersion curve calculated from an earth model (Steidl, 1997). Light error bar represents ± 1 standard deviation (std) of the phase velocity; heavy error bar represents ± 1 standard error of the mean (seom). Phase velocities obtained at the same site by the SASW method (Brown, 1998) are also included for comparison.
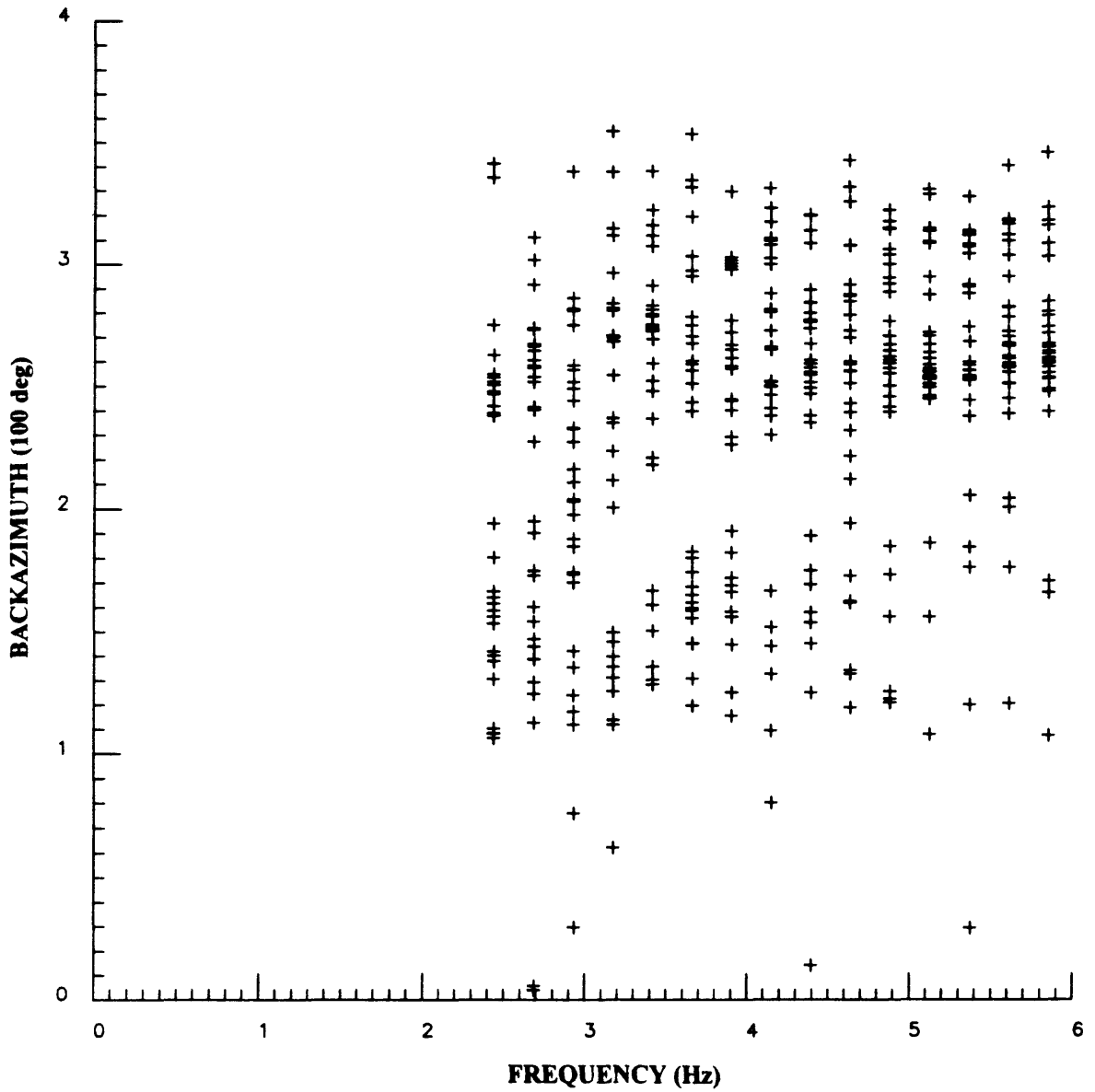
Figure 8a. Back azimuth of the highest peak of contour plots by the HRFK method from 31 separate time segments recorded by the Garner-Valley array.
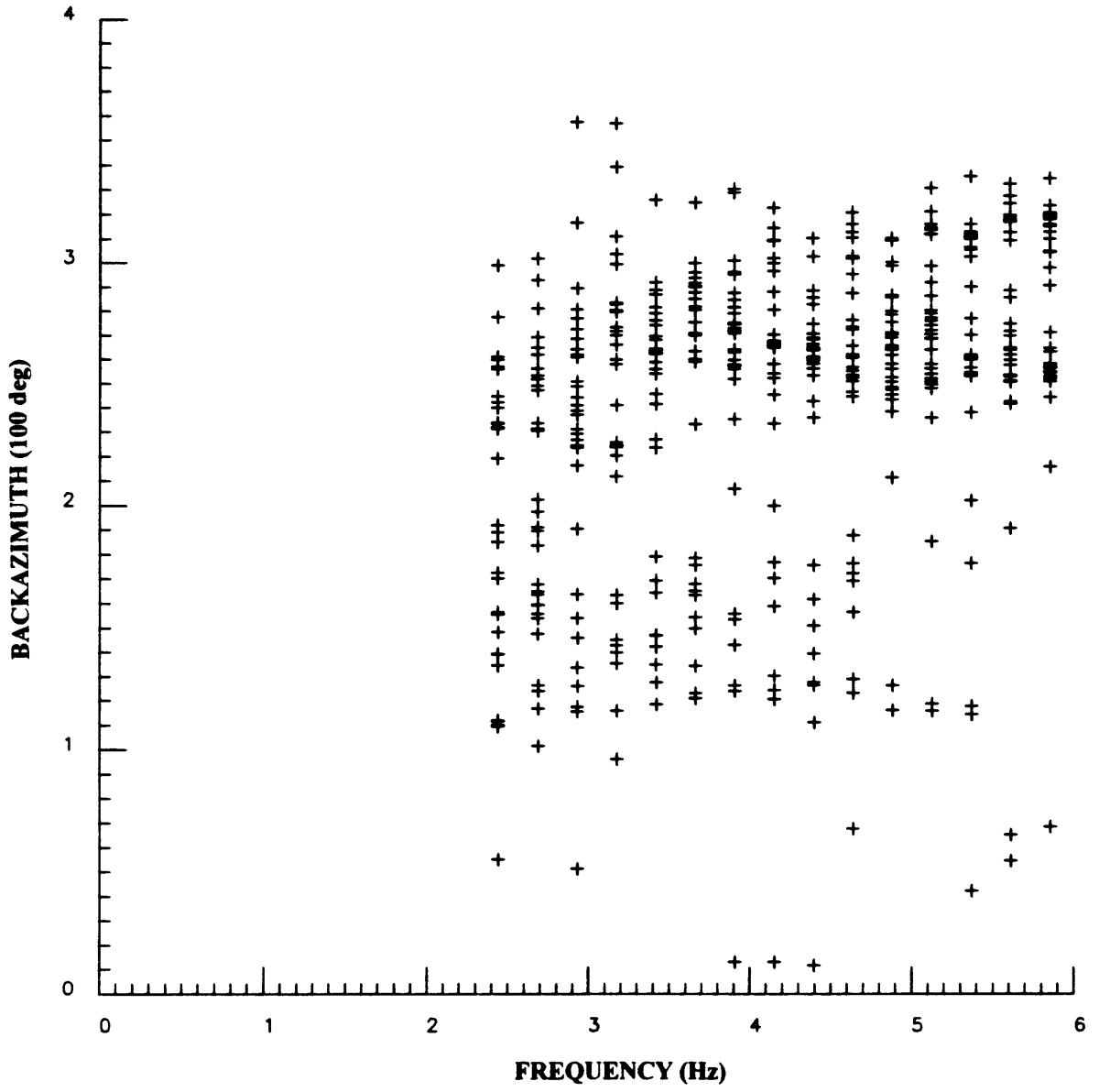
Figure 8b. Back azimuth of the highest peak of contour plots by the BF method from 31 separate time segments recorded by the Garner-Valley array.
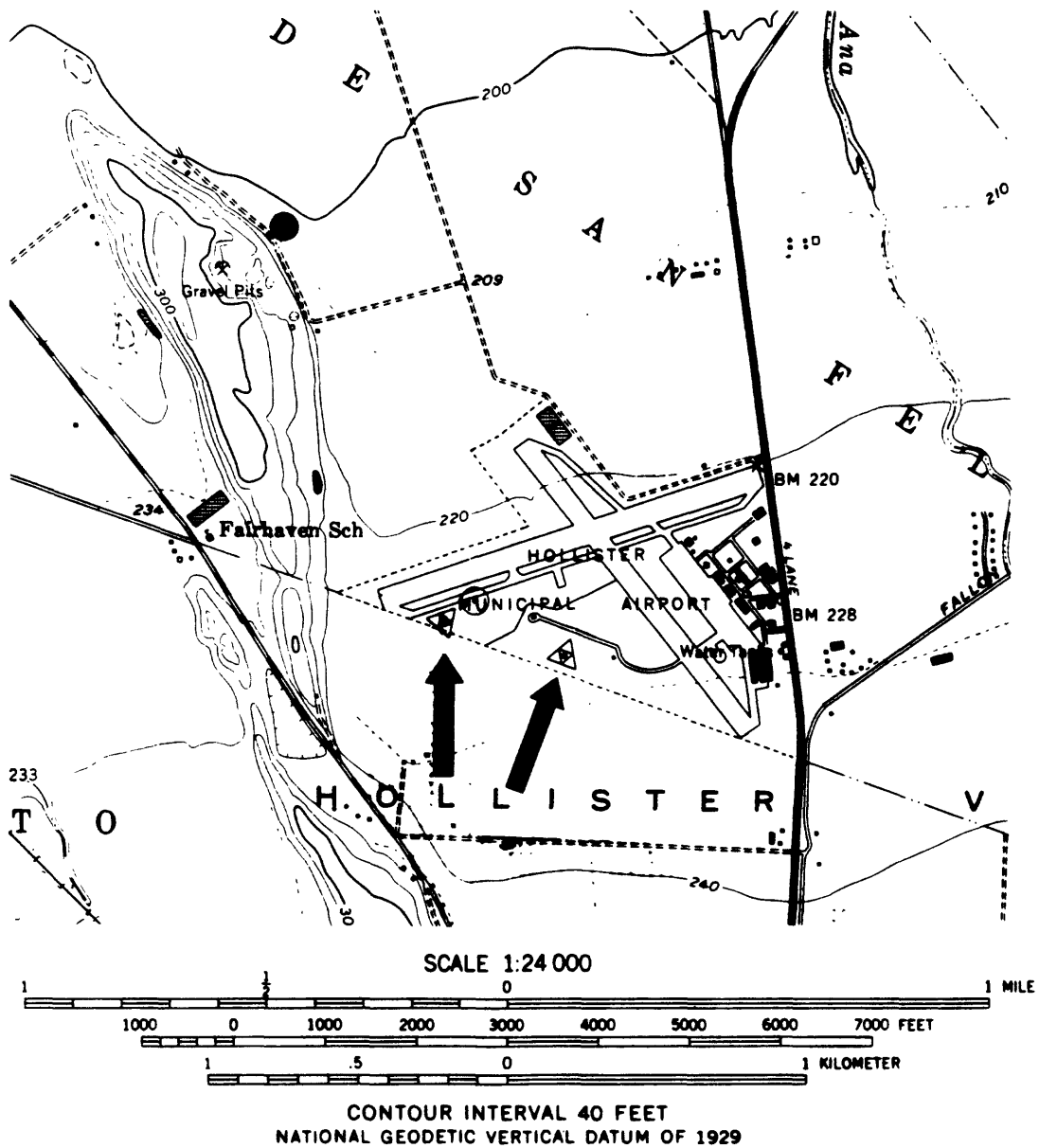
Figure 9. Array locations at the Hollister Municipal Airport (each pointed by an arrow) and location of the 60-m deep borehole (dot with a circle) where downhole velocity logs were obtained. Array #1 is to the east of Array #2. A solid circle near a pressure ridge of the Calaveras fault indicates an oil and gas test well that reached bedrock at ~1,200-m depth.

31
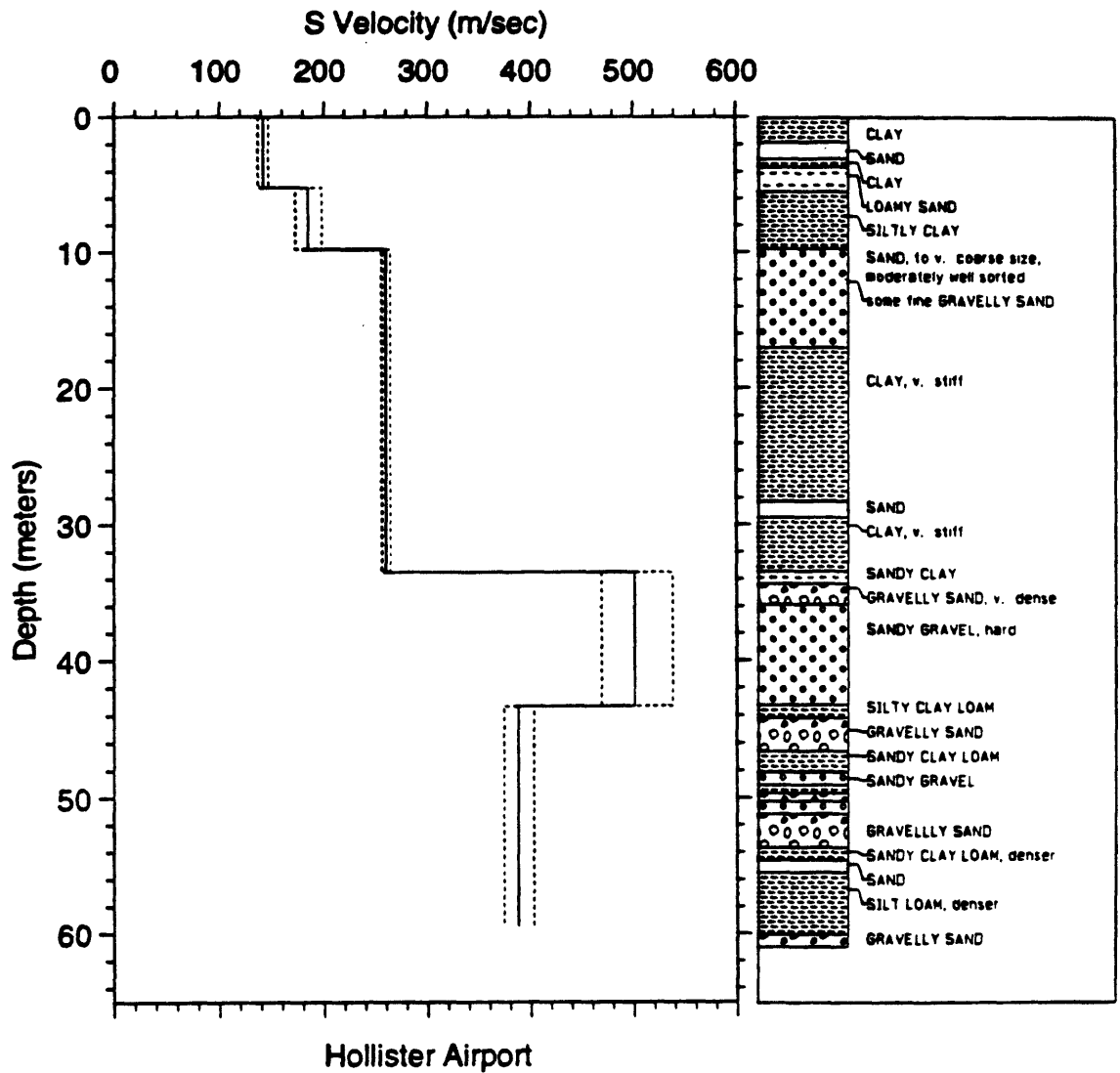
Figure 10. Shear-wave-velocity profiles (light dashed lines representing plus and minus one standard deviation) and simplified geologic log obtained from a borehole at the Hollister Municipal Airport ~70 m from the northeast tip of Array #2.
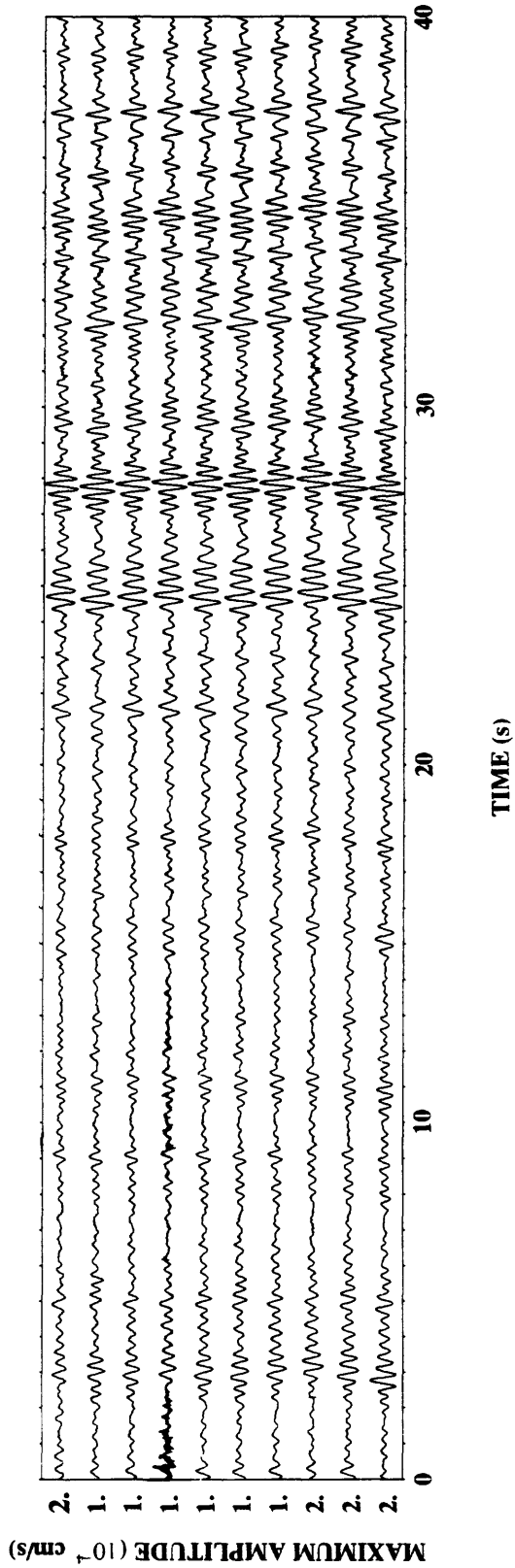
Figure 11*a*. Microtremor recorded by Array #1 at the Hollister Municipal Airport. These records are very similar to each other.

33
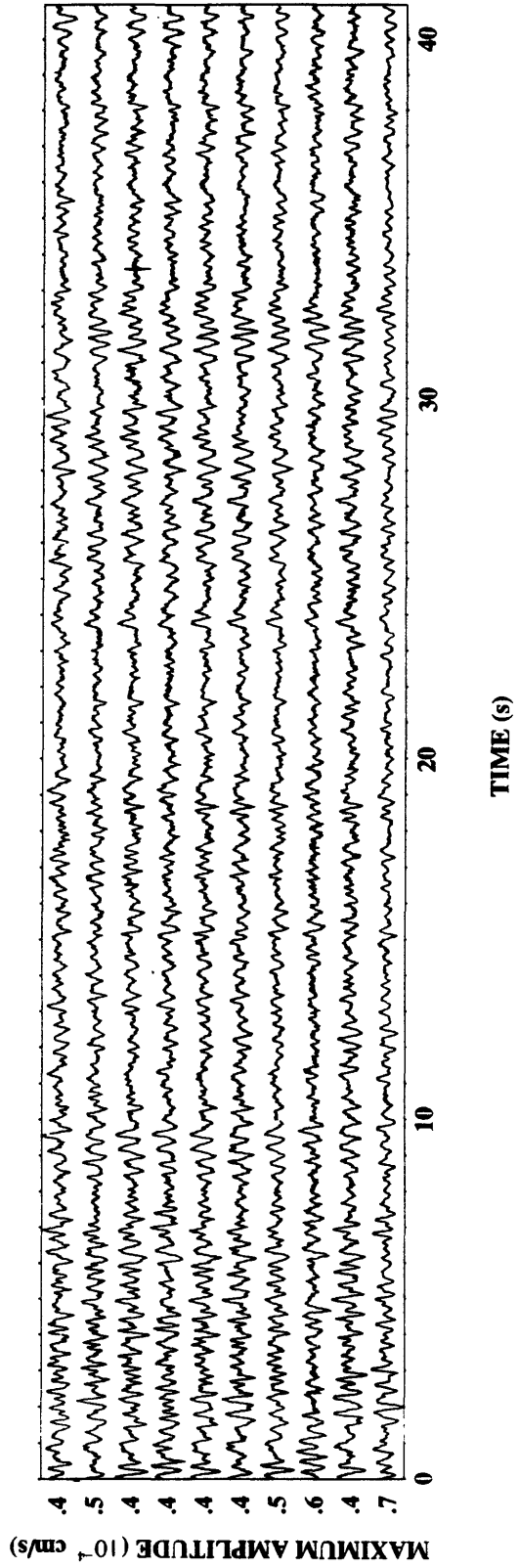
Figure 11b. Another set of microtremor recorded by Array #1 at the Hollister Municipal Airport. These records, although less similar to each other, are more representative of the data set.

34
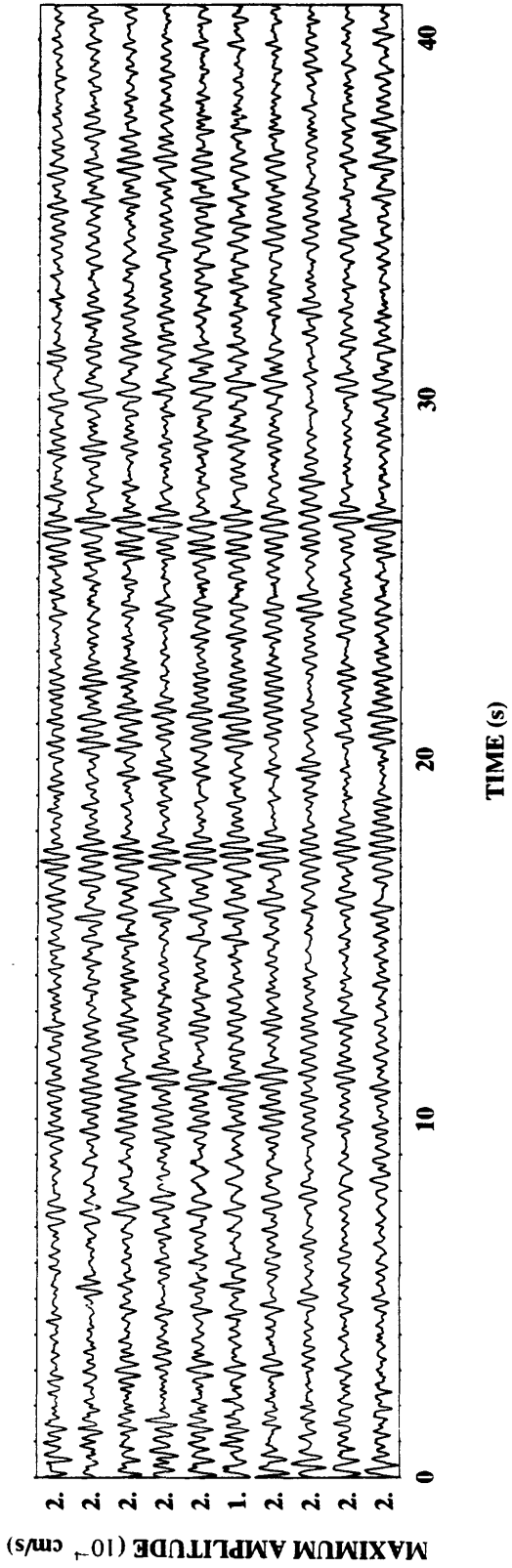
Figure 11c. Sample microtremor recorded by Array #2 at the Hollister Municipal Airport.

35
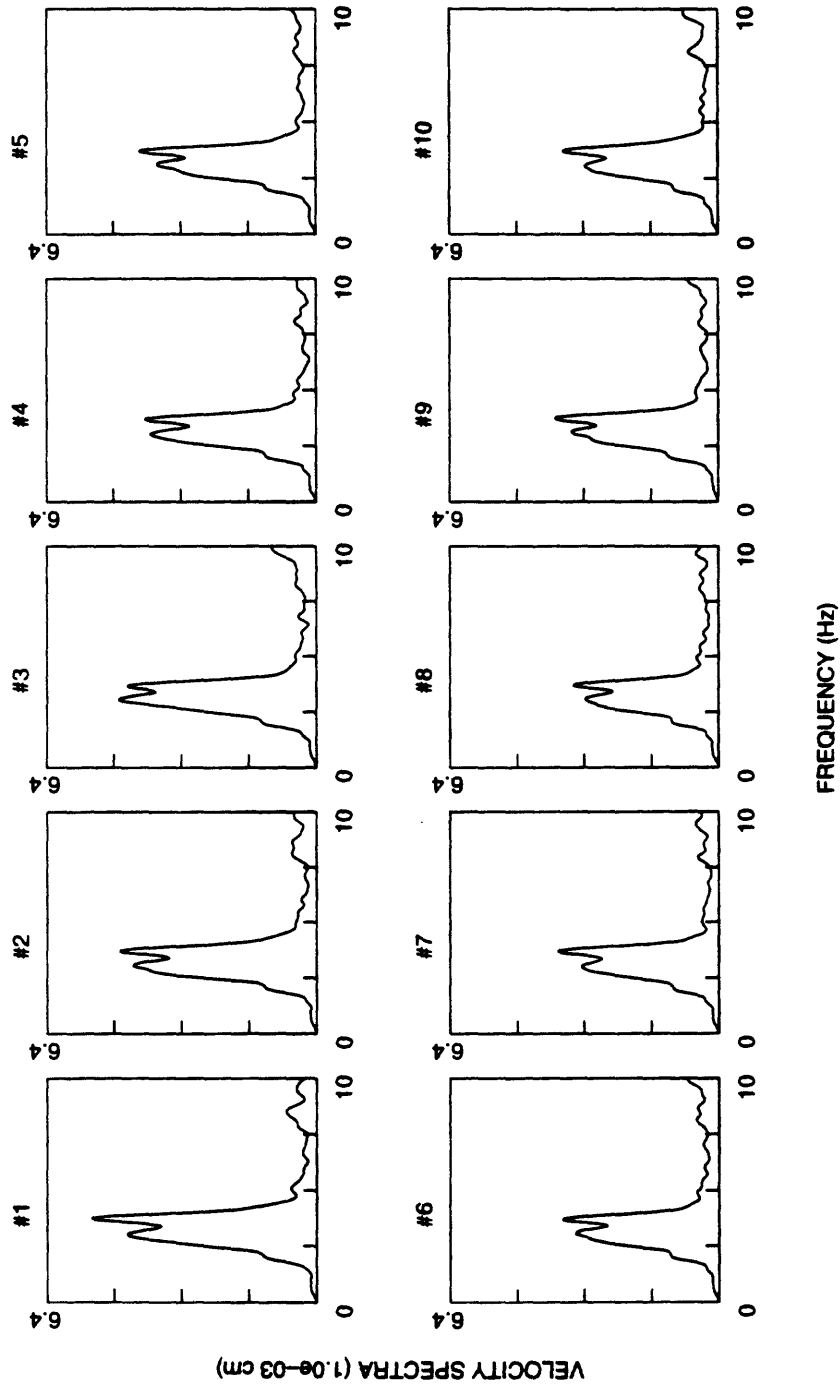
Figure 12. Fourier spectra of the microtremor records obtained at Array #1 in September of 1995 and shown in Figure 11a.
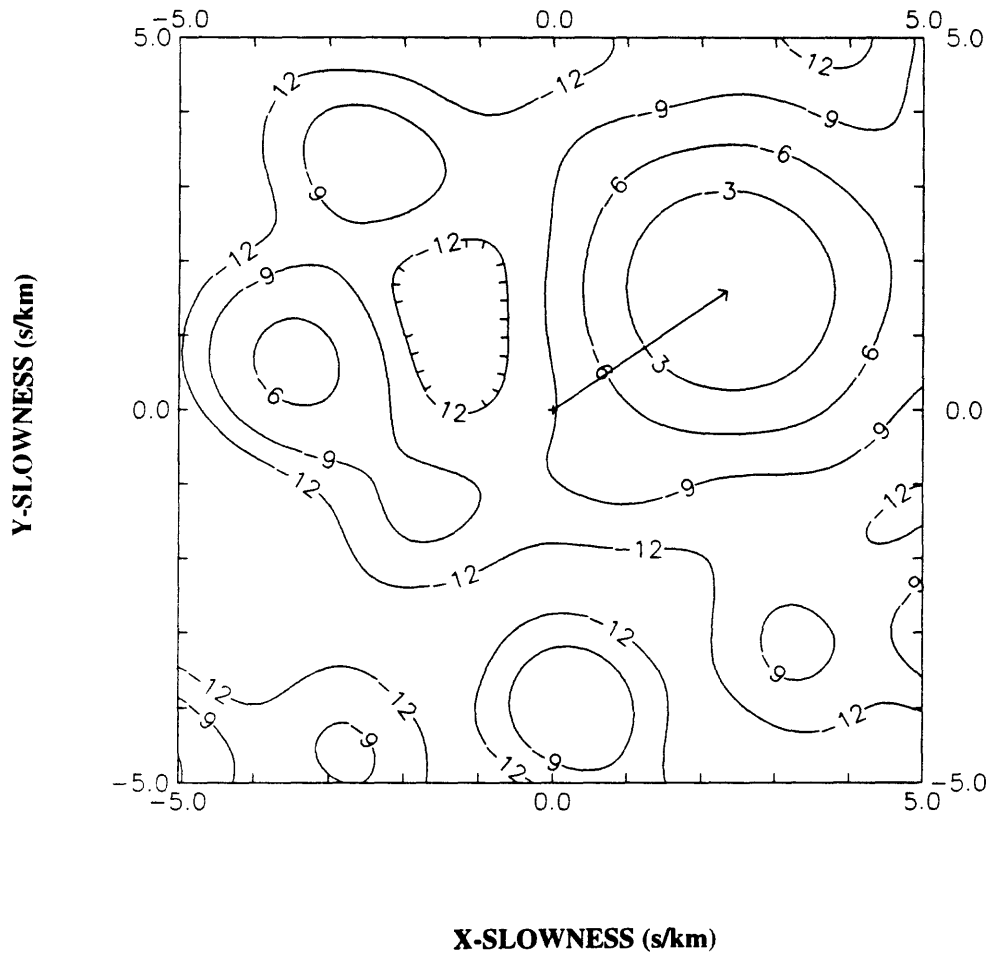
Figure 13a. Contour plot of $\left|\hat{P}\left(s_x, s_y, \omega\right)\right|$ in the s_x - s_y plane by the BF method at 3.91 Hz for the beam output formed from the microtremor records shown in Figure 11a (contour interval 3 dB).
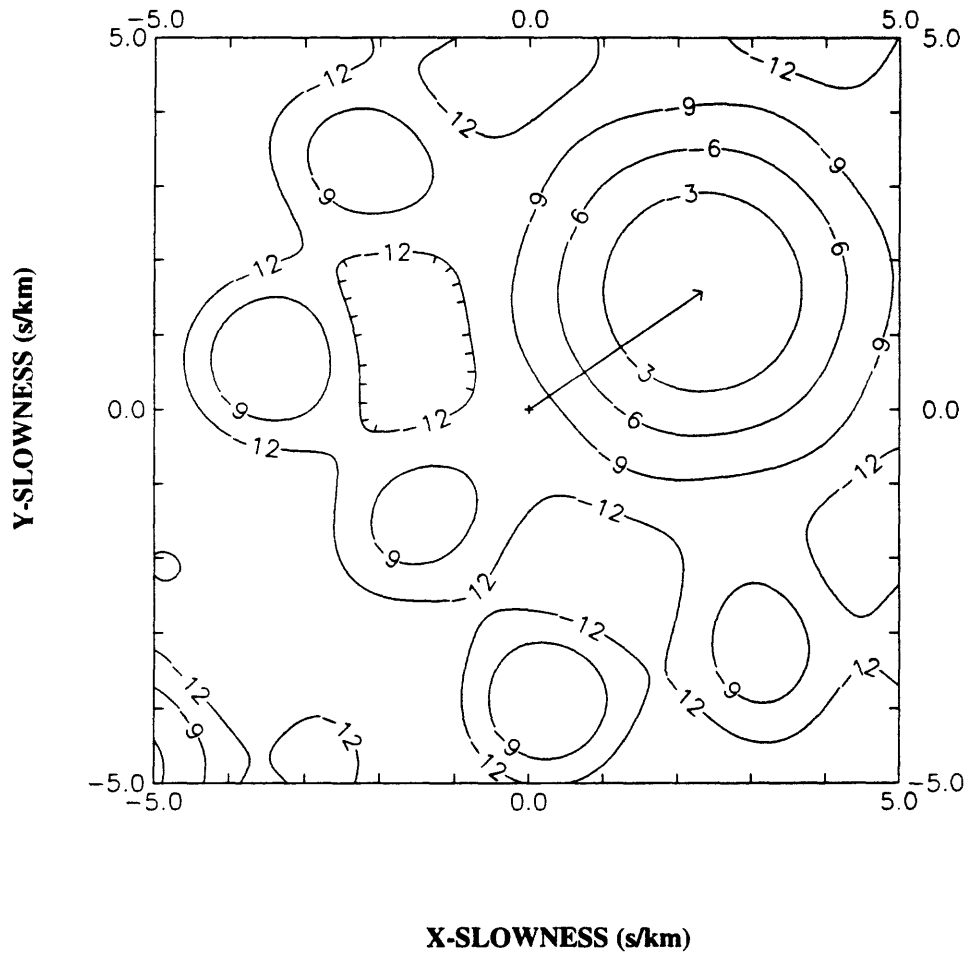
Figure 13*b*. Theoretical contour plot of $\left|\hat{P}\left(s_x, s_y, \omega\right)\right|$ by the BF method at 3.91 Hz for plane waves with slowness $s = 2.85\,\text{s}/\text{km}$ and back azimuth $\psi = 56°$ (values determined from Figure 13*a*).
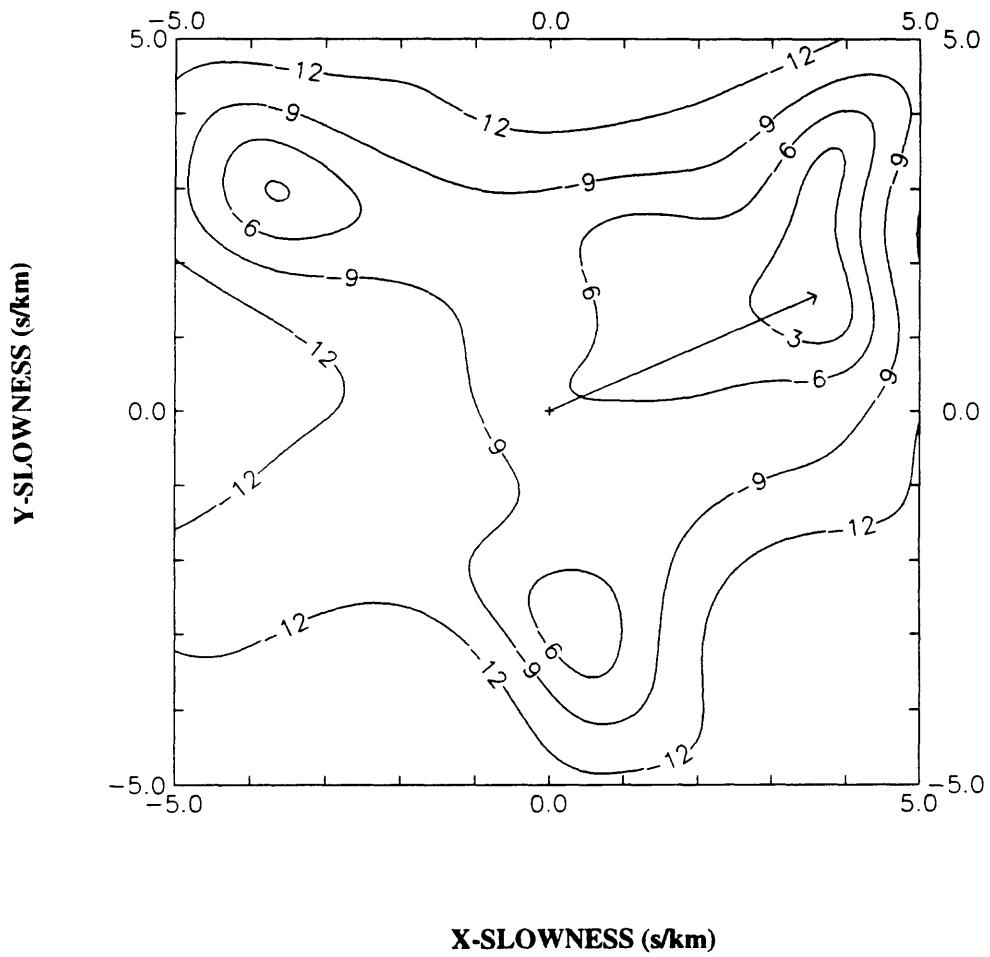
Figure 13c. Contour plot of $\left|\tilde{P}(s_x, s_y, \omega)\right|$ calculated by the HRFK method at 3.91 Hz from the microtremor records shown in Figure 11a (contour interval 3 dB).
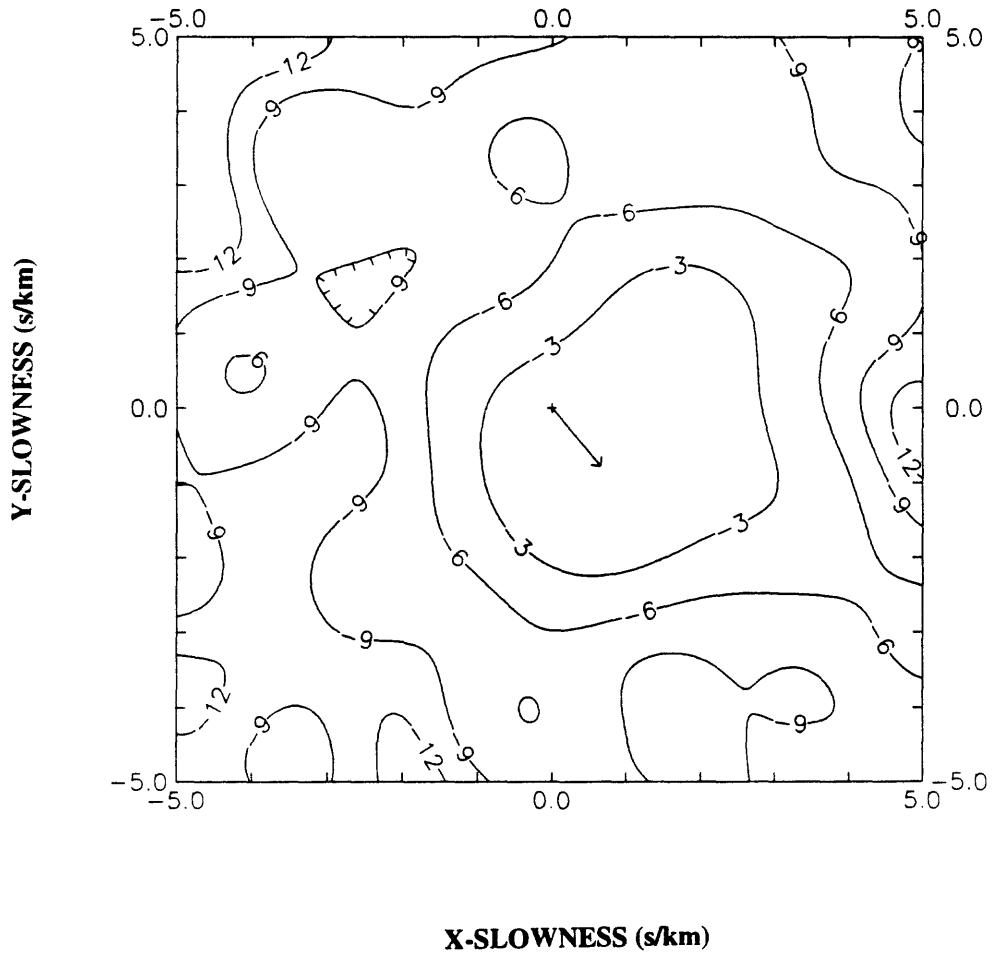
Figure 14a. Contour plot of $\left|\hat{P}(s_x, s_y, \omega)\right|$ by the BF method at 3.91 Hz for beams formed from the microtremor records shown in Figure 11b (contour interval 3 dB).
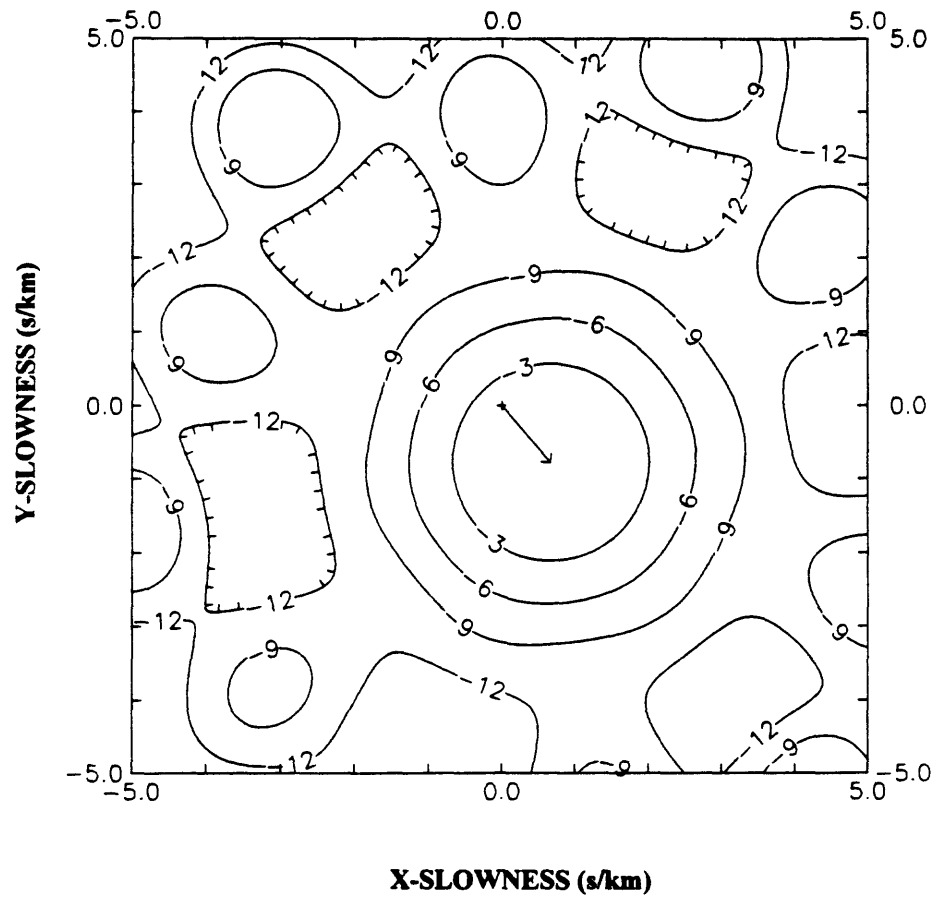
Figure 14*b*. Theoretical contour plot of $\left|\hat{P}(s_x, s_y, \omega)\right|$ at 3.91 Hz for plane waves with slowness $s = 1.01\,\text{s}/\text{km}$ and back azimuth $\psi = 139.7°$ (values determined from Figure 14*a*).
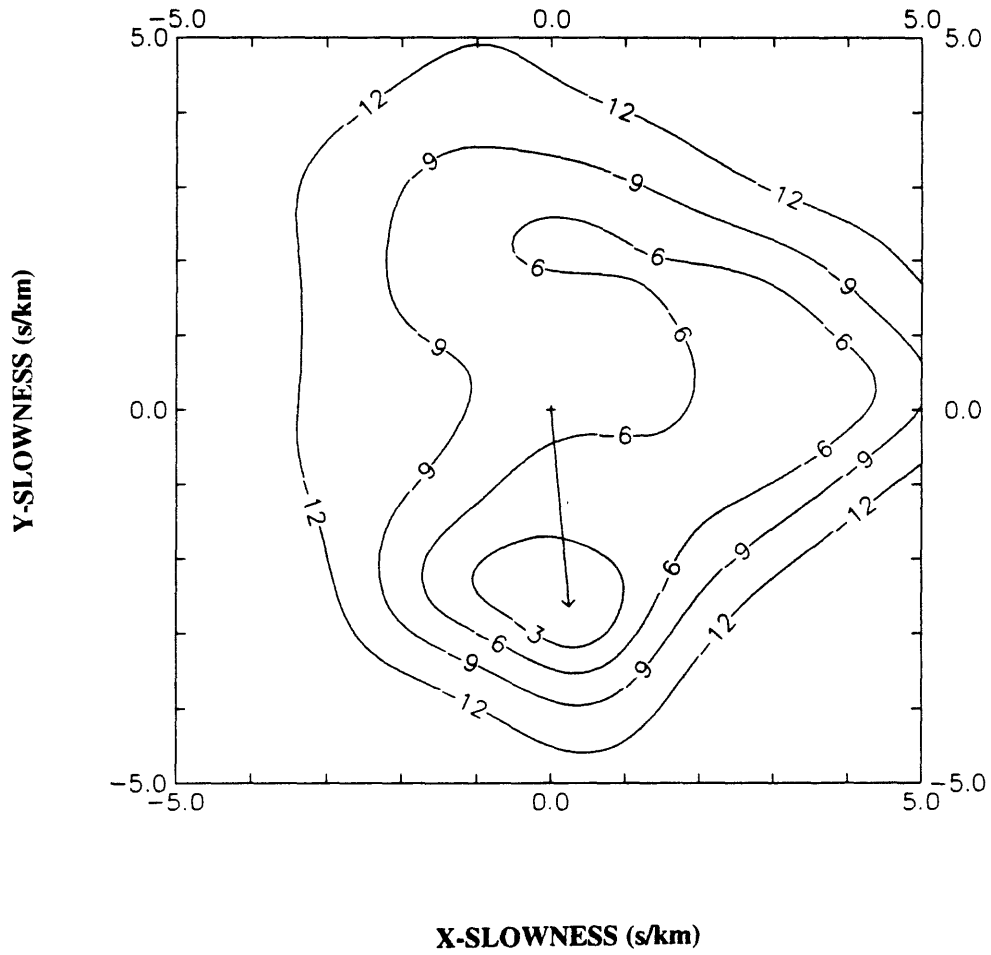
Figure 14c. Contour plot of $\left|\tilde{P}(s_x, s_y, \omega)\right|$ calculated by the HRFK method at 3.91 Hz from the microtremor records shown in Figure 11b (contour interval 3 dB).
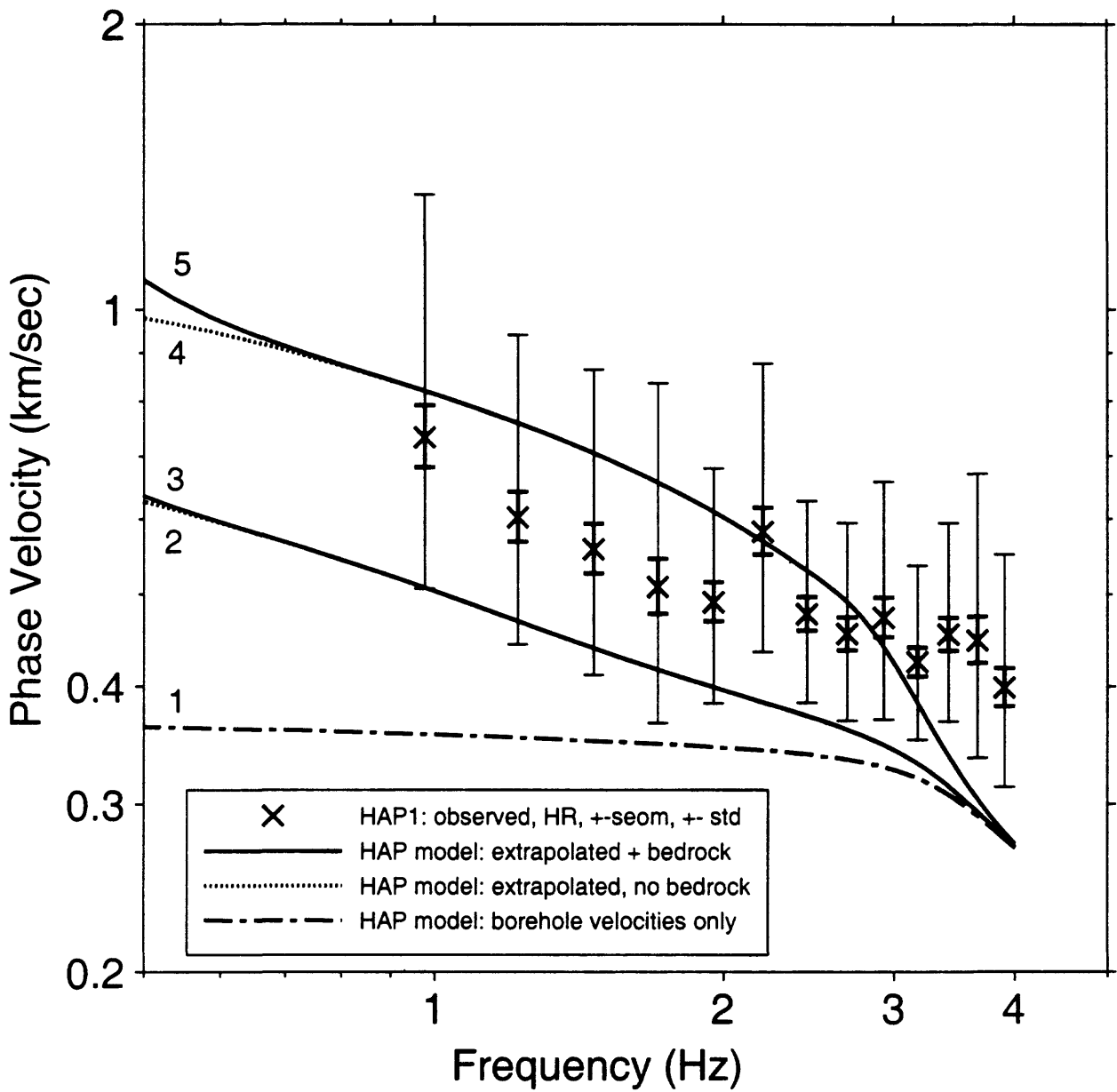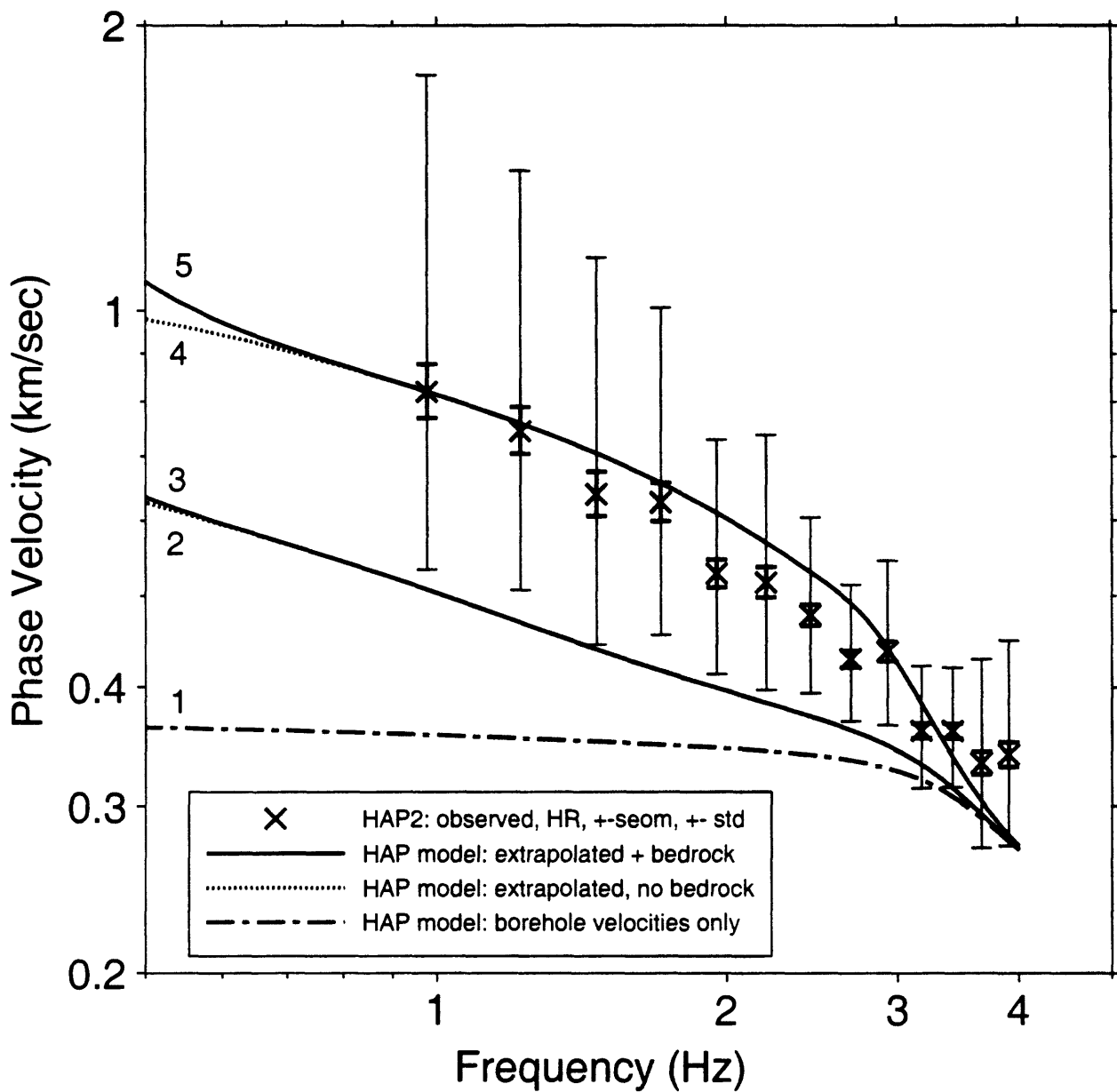
Figure 15a. Phase velocities determined from 35 separate time segments from Array #1 at the Hollister Airport by the HRFK method (light error bar represents ± 1 standard deviation of the phase velocity and heavy error bar represents ± 1 standard deviation of the mean). The dispersion curves are calculated from earth models constructed from borehole logging data and site geologic information (see text). Dispersion curve #2 is barely visible because of our choice of 0.5 Hz as the lower limit of the frequency axis.
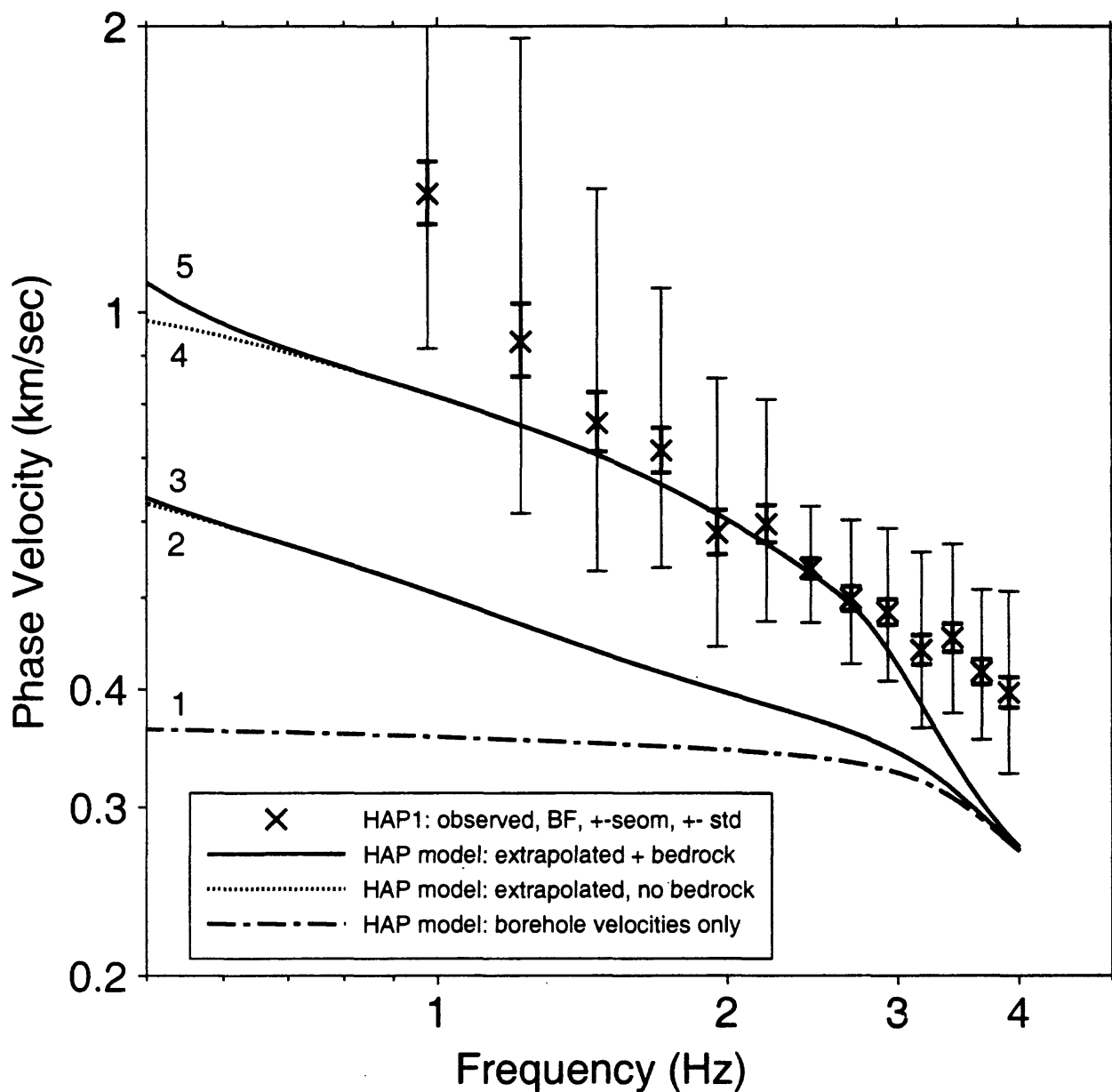
Figure 15*b*. Phase velocities determined from 35 separate time segments from Array #1 at the Hollister Airport by the BF method (light error bar represents ± 1 standard deviation of the phase velocity and heavy error bar represents ± 1 standard deviation of the mean). The dispersion curves are calculated from earth models constructed from borehole logging data and site geologic information (see text). Dispersion curve #2 is barely visible because of our choice of 0.5 Hz as the lower limit of the frequency axis.
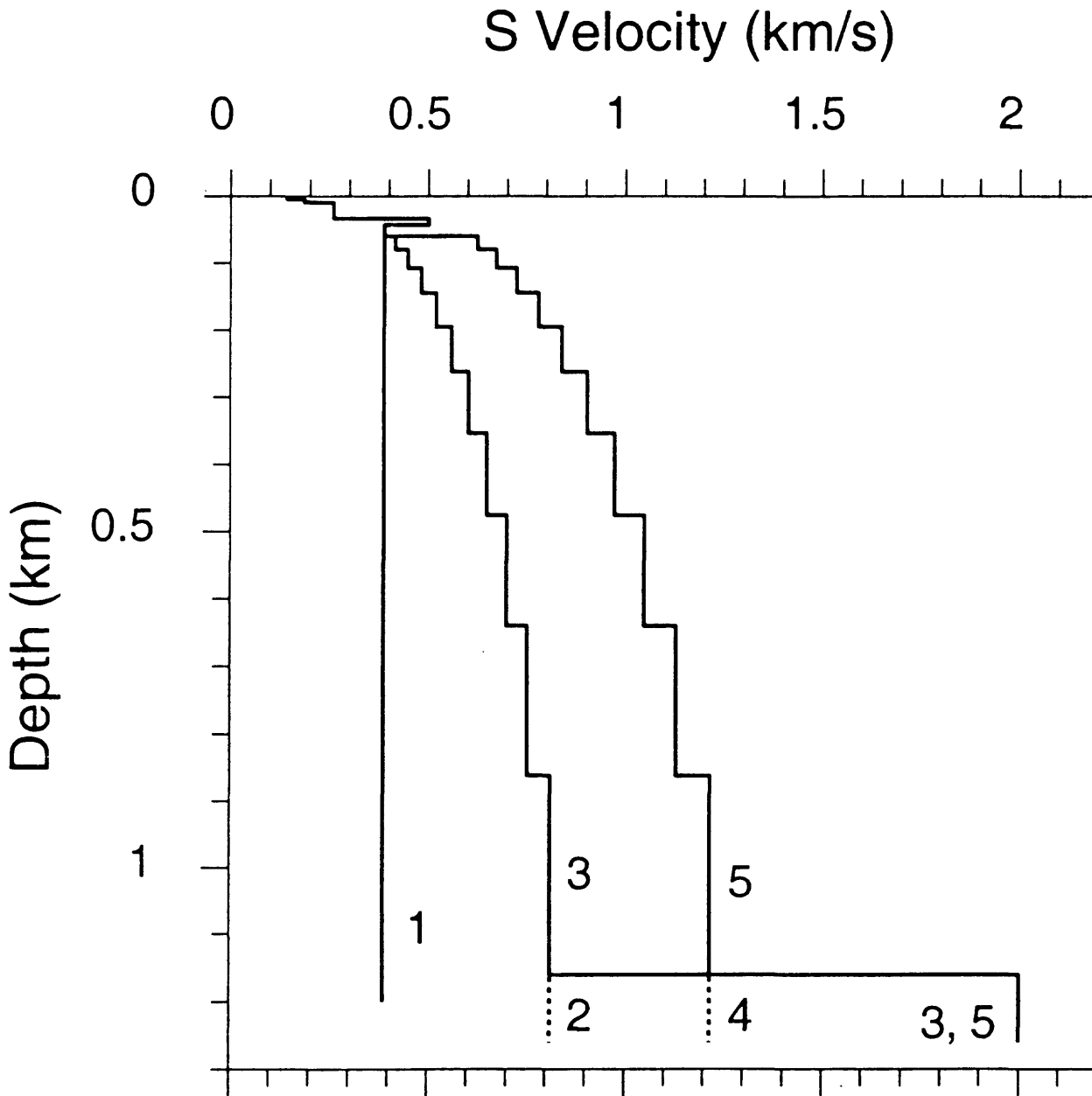
Figure 16. V_S models for calculating fundamental-mode Rayleigh-wave dispersion curves in Figure 15. V_S for the top 60 m are obtained from the borehole logging data (see Figure 10). V_S estimates for lower depths to 1160 m (a lower estimate to the left and an upper estimate to the right) are guided by the geologic information from Kilburn (1972) and the velocity information from Yamamizu and Goto (1978) and Yamamizu et al. (1981). Bedrock V_S is estimated to be 2.0 km/s.

Figure 17a. Phase velocities determined from 67 separate time segments from Array #2 at the Hollister Airport by the HRFK method (light error bar represents ± 1 standard deviation of the phase velocity and heavy error bar represents ± 1 standard deviation of the mean). The dispersion curves are calculated from earth models constructed from borehole logging data and site geologic information (see text).
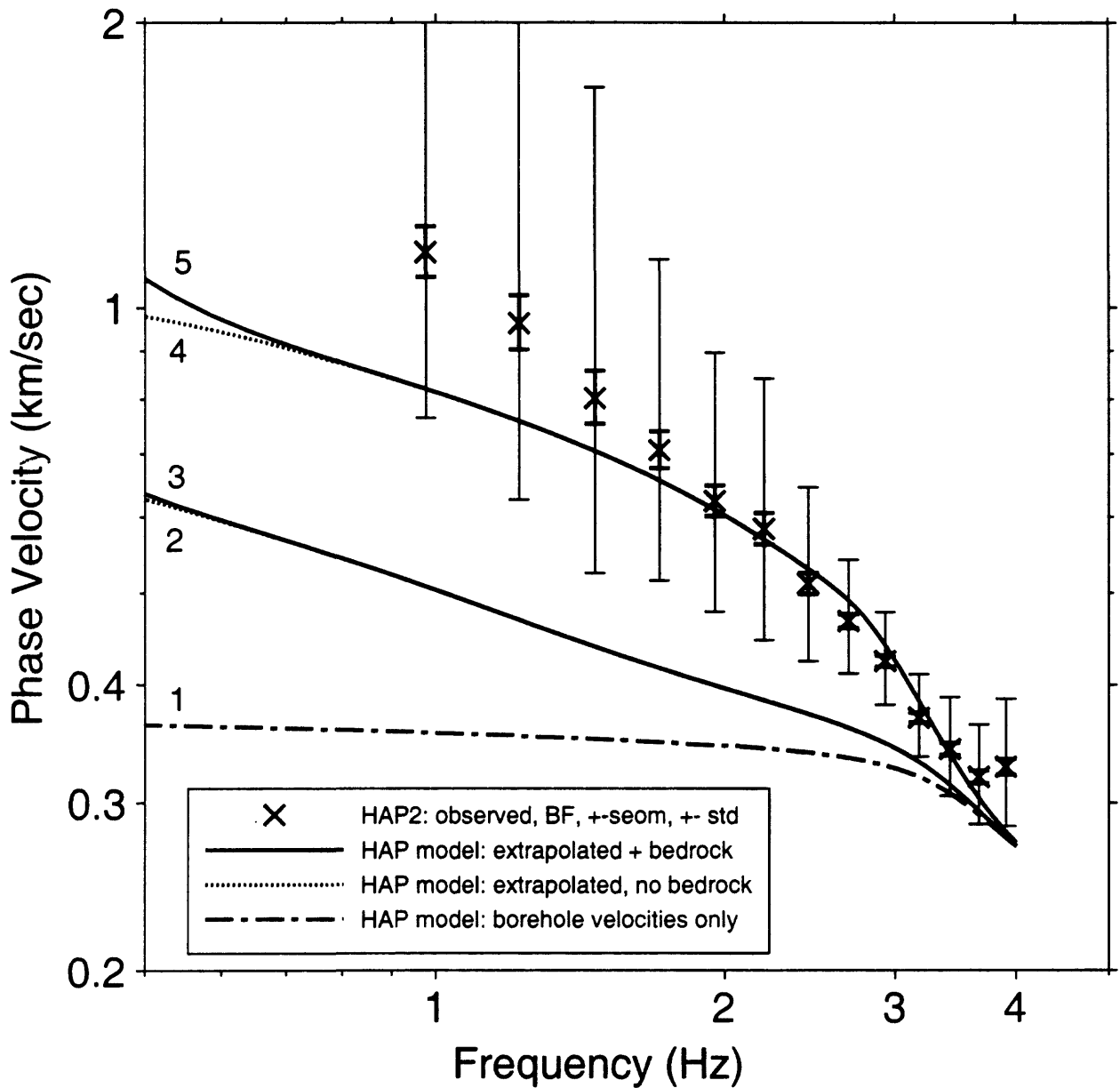
Figure 17*b*. Phase velocities determined from 67 separate time segments from Array #2 at the Hollister Airport by the BF method (light error bar represents ± 1 standard deviation of the phase velocity and heavy error bar represents ± 1 standard deviation of the mean). The dispersion curves are calculated from earth models constructed from borehole logging data and site geologic information (see text).
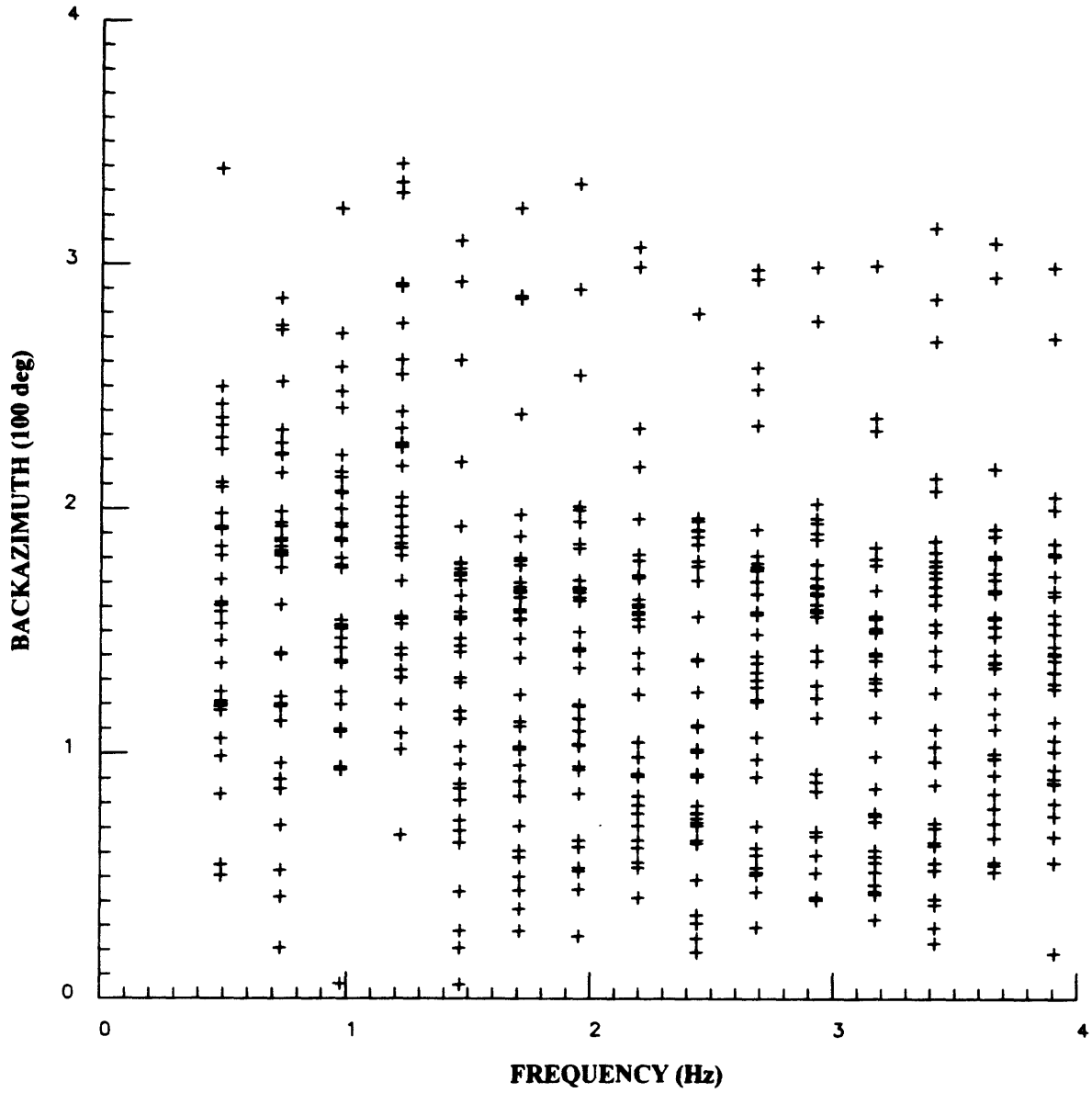
Figure 18a. Back azimuth of the peak in the measured power-spectral contour plots for Array #1 by the BF method.
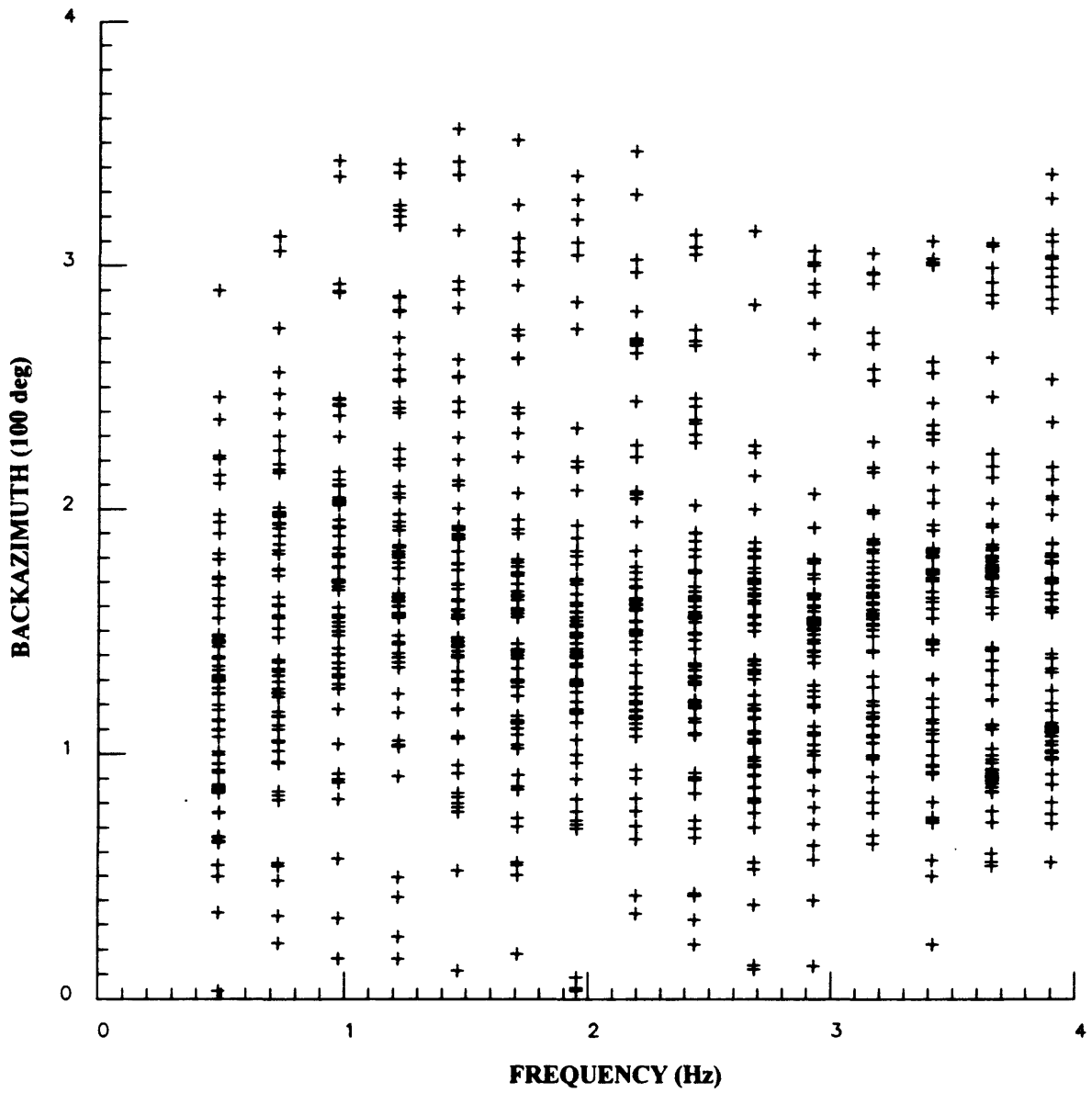
Figure 18*b*. Back azimuth of the peak in the measured power-spectral contour plots for Array #2 by the BF method.
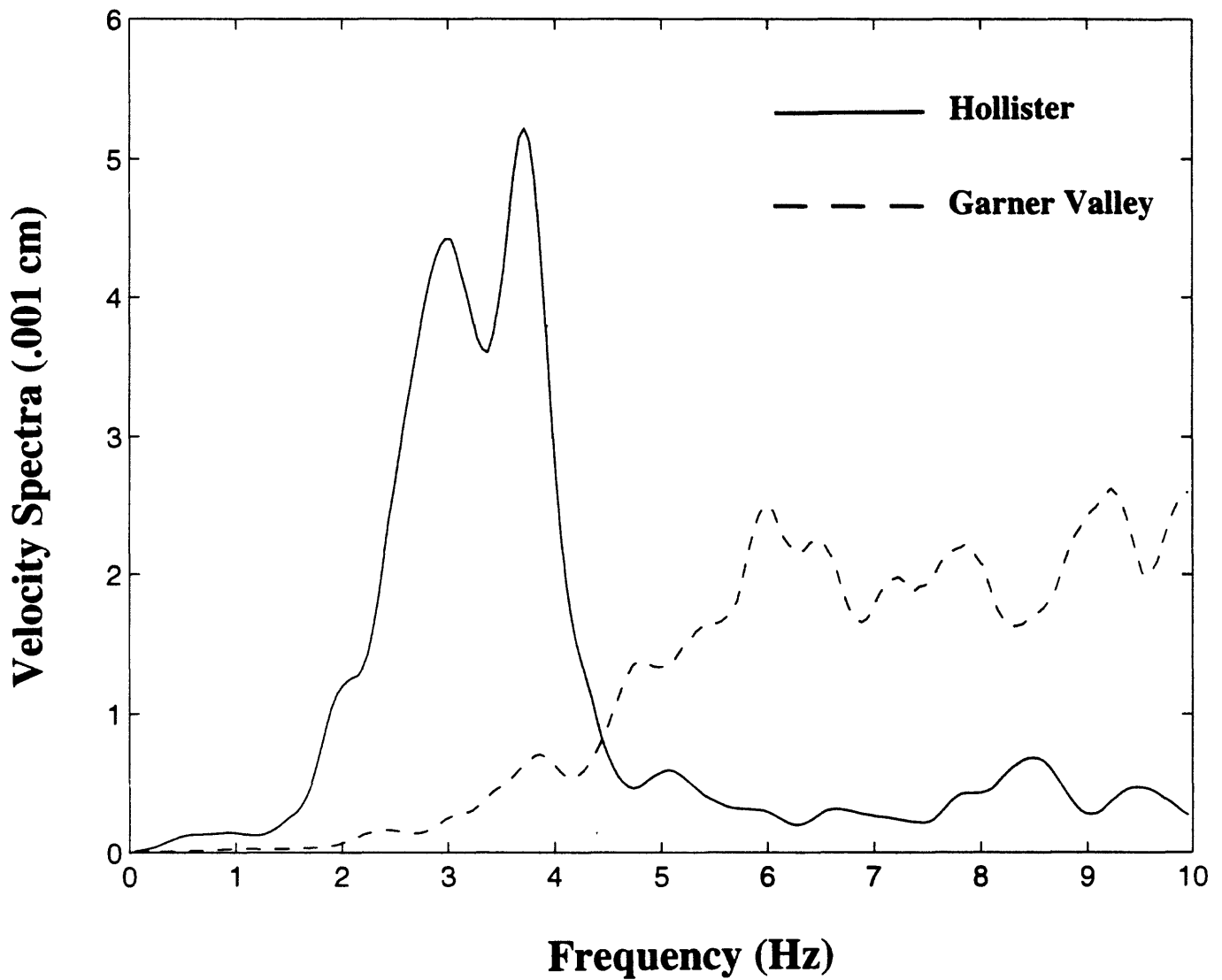
Figure 19. Comparison of microtremor spectra observed at Garner Valley and at Hollister. The Garner Valley spectrum has higher frequency content.
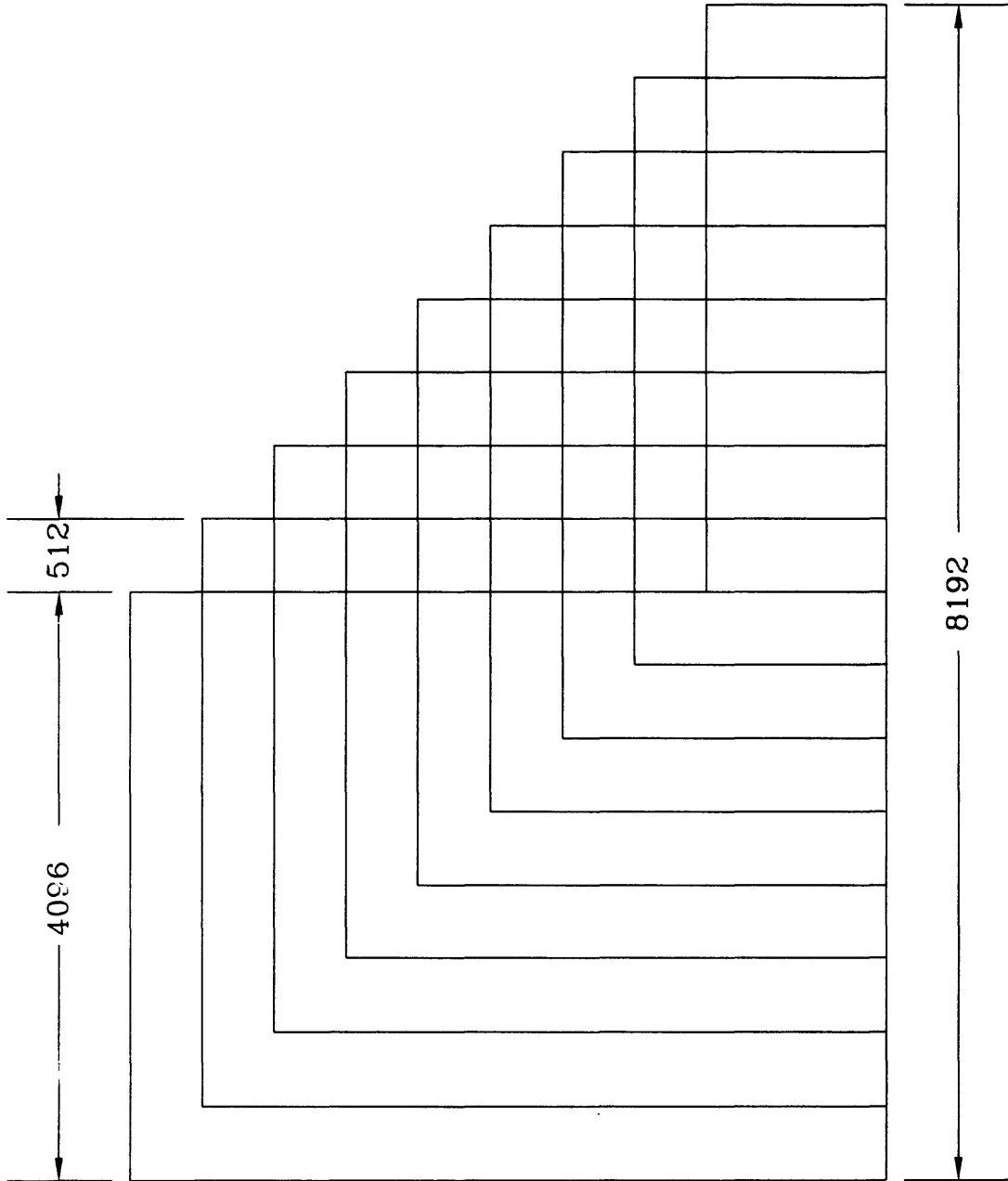
Figure A1. Sample-averaging scheme for the beam-forming method: a seismogram of 8192 samples (40.96 s long) is divided into nine overlapping sections as shown.
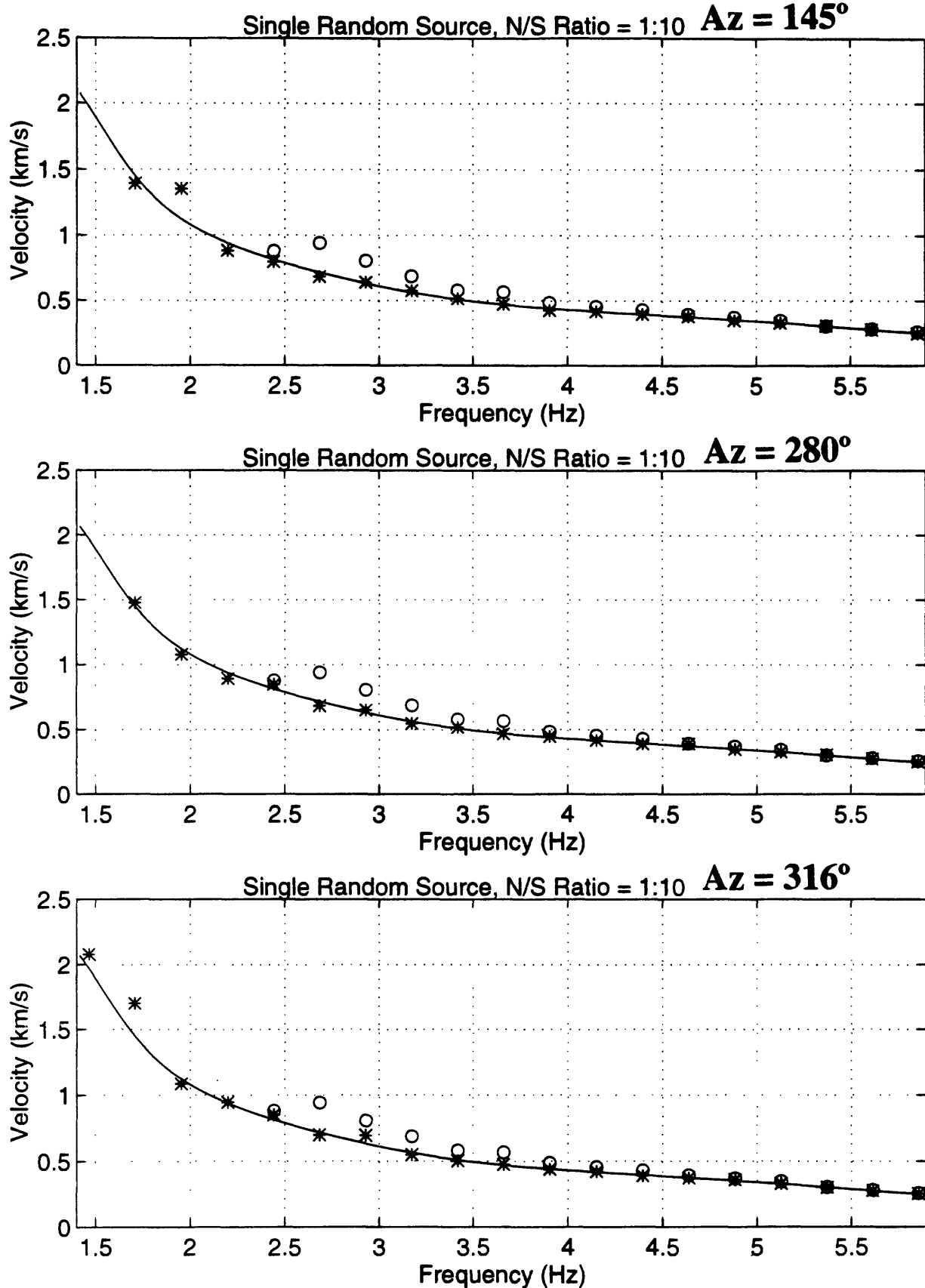
Figure B1. Phase velocities from power-spectral calculation for synthetic ground noise simulating a single plane wave for the Garner-Valley array configuration (stars). The plane wave travels at the calculated phase velocity (solid curve) at the indicated frequency; back azimuth of the plane wave is indicated on top of each plot. Mean values of phase velocities from field measurements (circles) are shown for comparison.
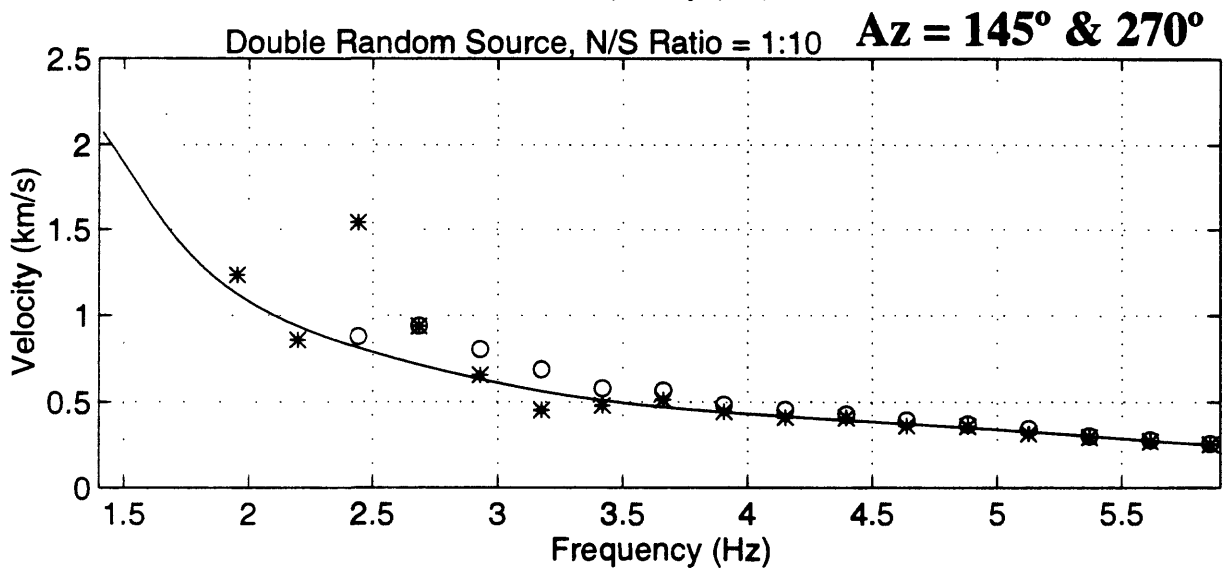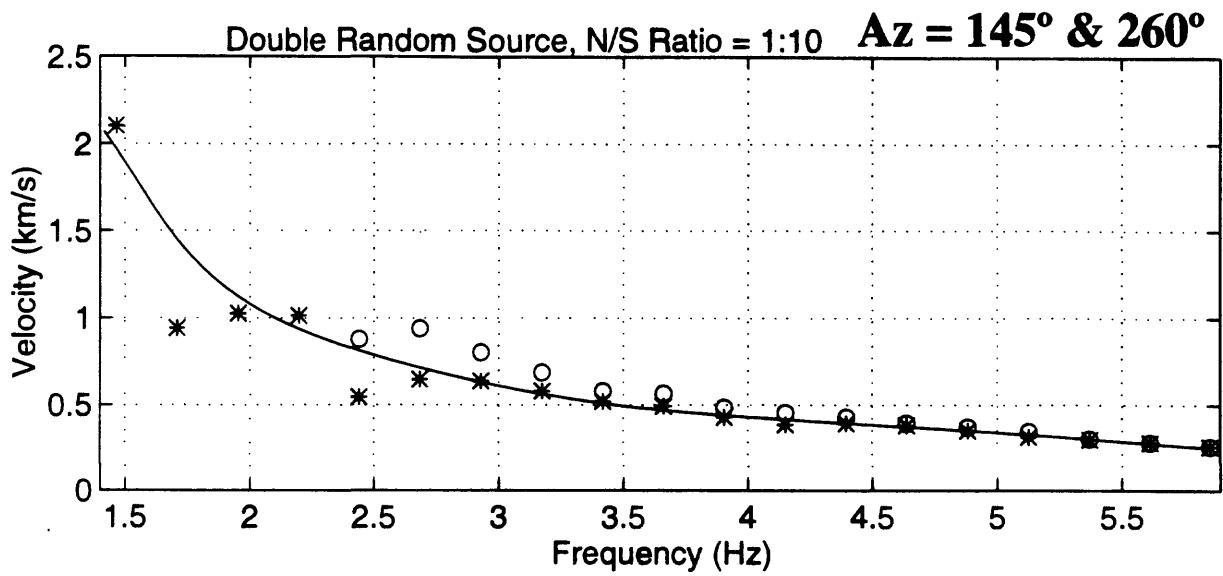
52
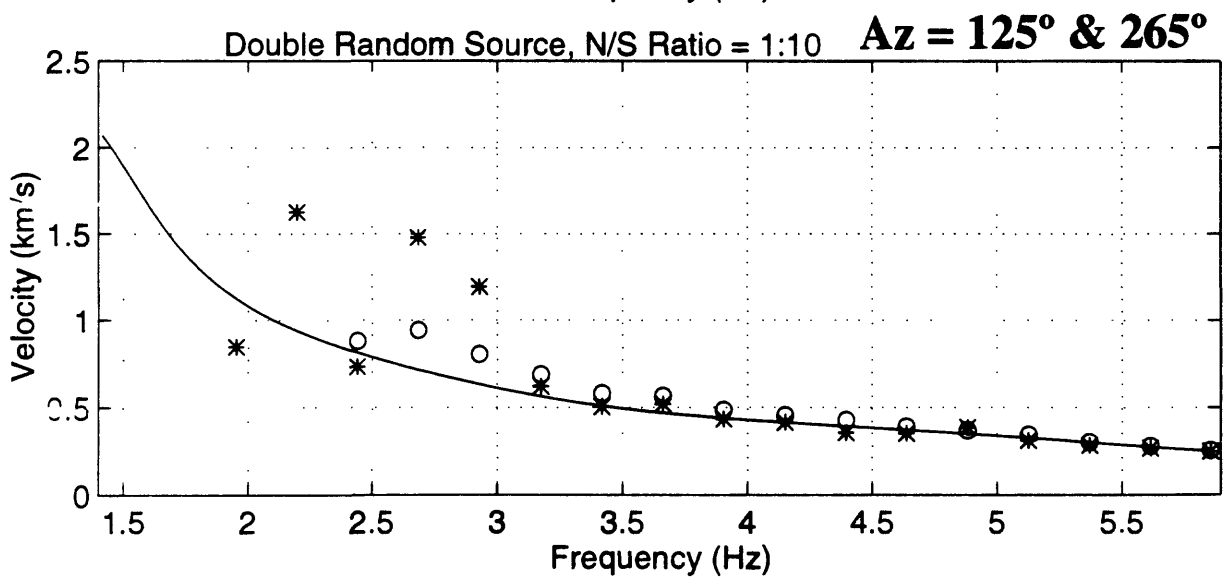
Figure B2. Similar to Figure B1 except that there are two plane waves. Back azimuths of the plane waves are indicated on top of each plot.
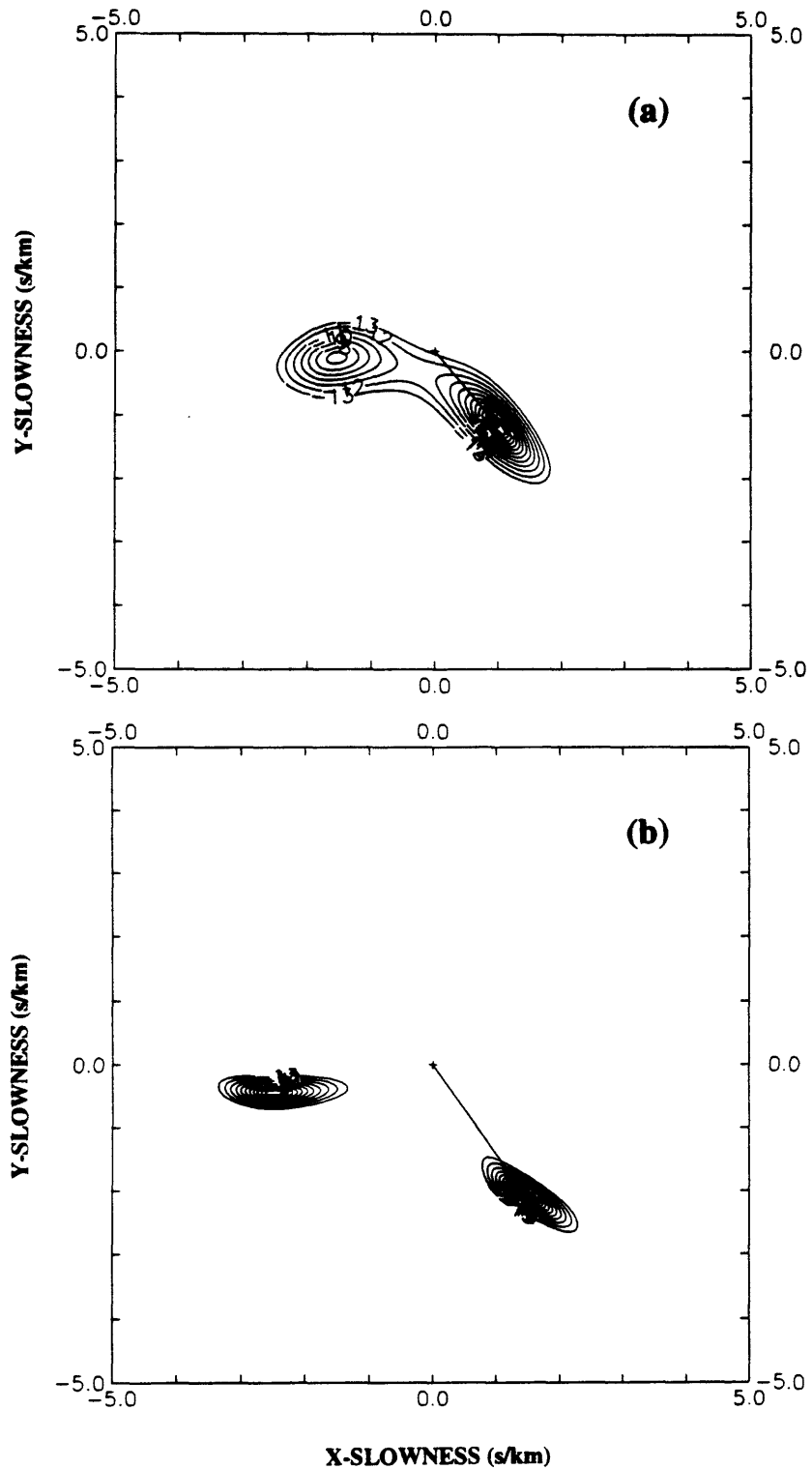
Figure B3. Power spectrum contours (a) at 2.9 Hz, and (b) at 4.4 Hz, for two synthetic ground noise that generated the results shown in Figure B2.